Contactless electrostatic shaping of a capillary jet for drop-on-demand purposes

Samy Lalloz, Laurent Davoust

To cite this version:

Samy Lalloz, Laurent Davoust. Contactless electrostatic shaping of a capillary jet for drop-on-demand purposes. Physics of Fluids, 2022, 34 (1), ⟨10.1063/5.0076605⟩. ⟨hal-04909117⟩

Contactless electrostatic shaping of a capillary jet for drop-on-demand purposes

Samy Lalloz[1] and Laurent Davoust[2, a)]

1) *Electromagnetic Processing of Materials (EPM) Group,*
Materials and Processes Science and Engineering Laboratory (SIMaP),
Grenoble Institute of Technology (Grenoble-INP)/Univ. Grenoble-Alpes/CNRS,
38402 Saint Martin d'Hères, France

b)

2) *Electromagnetic Processing of Materials (EPM) Group,*
Materials and Processes Science and Engineering Laboratory (SIMaP),
Grenoble Institute of Technology (Grenoble-INP)/Univ. Grenoble-Alpes/CNRS,
38402 Saint Martin d'Hères, France

(Dated: Submitted: November 27, 2021/ Received: date / Accepted: date)

The contactless electrostatic shaping of a capillary jet can be adjusted so as to generate a monodisperse spray in the jetting regime. To demonstrate this, an actuator based on stacked electrodes is developed to generate a spatially modulated electric stress. The latter promotes the parametric excitation of a standing capillary wave along a capillary jet. The objective is to control its breakup length and to phase lock the drop ejection. Experiments are carried out based on light absorption and fast imaging. The breakup length and the drop size distribution are measured. The comparison with a stability model allows us to identify resonant frequencies which monitor the size or the number density of drops. The concept of synchronization frequencies is introduced here with possible use in future developments of electrodynamic actuators. ~~electrosprays~~

---

a) Electronic mail: Corresponding author: laurent.davoust@simap.grenoble-inp.fr.

b) Electronic mail: samy.lalloz@lncmi.cnrs.fr

I. INTRODUCTION

In various applications such as coating technologies, inkjet printing[1–4], 3-D printing, micropowders production, bioanalysis (mass spectrometry) or biomicrofluidics (digital lab-on-a-chips)...etc, a generic challenge is to produce on-demand drops as monodisperse as possible. To meet this challenge, various strategies have been proposed for the development of drop-on-demand dispensers based on a capillary jet, a pendant drop, a sessile drop or a meniscus: acoustofluidics[5,6], pneumatic actuation[7], electrohydrodynamics[8–16], electrowetting[17–23]...etc, but one of the most widely used today relies on the electro-acoustic (piezoelectric) atomisation of a liquid sample[24–34]. The latter strategy originates from pioneering Rayleigh's work on the capillary destabilization of a capillary jet[35]. A sound wave is generated from a piezoelectric system put in contact with the liquid to be atomised, the latter being ejected from the orifice of a container in the form of a cylindrical capillary jet. The wave-induced alternating pattern of acoustic nodes and antinodes causes a series of radial disturbances along the jet. By carefully selecting the wavelength of the sound wave, *i.e.* the frequency of the signal applied to the piezoelectric device, it is possible to promote a Rayleigh-Plateau (RP) instability, which results in a train of drops with the suitable size. The latter obviously depends on the physicochemical properties of the fluid (density, surface tension), on the initial radius of the jet, on the input flow rate as well as on the frequency of the actuation applied.

This approach has clearly demonstrated its relevancy as illustrated by the amount of literature devoted to it. However, competitive strategies can be proposed, also based on capillary destabilisation, and which deserves to be further developed.

As briefly mentioned above, a good alternative is based on the use of electrohydrodynamics. This consists for instance in imposing an electric stress either at the apex of an electrified pending drop (dripping regime[36,37]) or at the surface of an electrified liquid jet (jetting regime[13,38,39]). This electric stress results from an interaction between an electric field, externally applied, streamwise or spanwise, and a surface density of electric charges arising all along the jet surface. It should be noted that the presence of these electric charges issues from the existence of a normal component of the electric field and from the existence of a jump in dielectric permittivity between the liquid jet and the ambient air[40]. The electric

field can be applied for instance from a ring electrode through which the liquid jet initially grounded or initially electrified can make its way[41]. These methods based on electrostatics have two immediate advantages over the electro-acoustic method. First of all, the electric actuator is not intrusive as long as it is not immersed in the liquid. Indeed, under normal conditions of use, the counter electrode must not be put in contact with the liquid so that the ambient air can play its role as a capacitor. A second advantage is the absence of wave reflections. In the electro-acoustic approach, acoustic waves can be reflected at the surface of the container. These reflected waves contribute to the excitation of parasitic modes. Among possible consequences, there is a complexification of the relation between the input signal frequency and the wave number of the capillary disturbance and, as a result, the generation of droplets with a unique size can be seriously challenged. This wave reflection phenomenon is not present with the electrostatic approach because the electric stress is directly applied at the interface.
The alternative technique proposed in the present paper differs in some extent from usual electrostatic actuation since, this time, it consists of imposing a standing wave of electrostatic pressure along the surface of the jet. The objective consists somewhat in electrostatically shaping the liquid jet so as to deform it in a contactless way as close as possible from the most unstable RP mode.

Apart from rare studies available in the literature[8,9,42], our approach has surprisingly never been investigated in full depth. Only a few configurations were tested with the sole objective of controlling the breakup length of a liquid jet. To the best of our knowledge, none study can be found in the literature dedicated to the development of a stacked-type electrostatic actuator and its ability to monitor the size distribution of the droplets after atomisation.

Here, some theoretical ingredients are given, based on the hypothesis of a slender-jet and the use of a linear stability model to deliver an estimate of the breakup length[43]. Experimental developments on the electrostatic destabilisation of a conductive liquid jet are described in details. After a presentation of the electrostatic actuator and the experimental methods used, a comparison with the stability model is carried out in order to clarify the link between the spatial periodicity of the electrode stack, the imposed frequency, the breakup length and the size distribution of the ejected drops.

II. LINEAR STABILITY

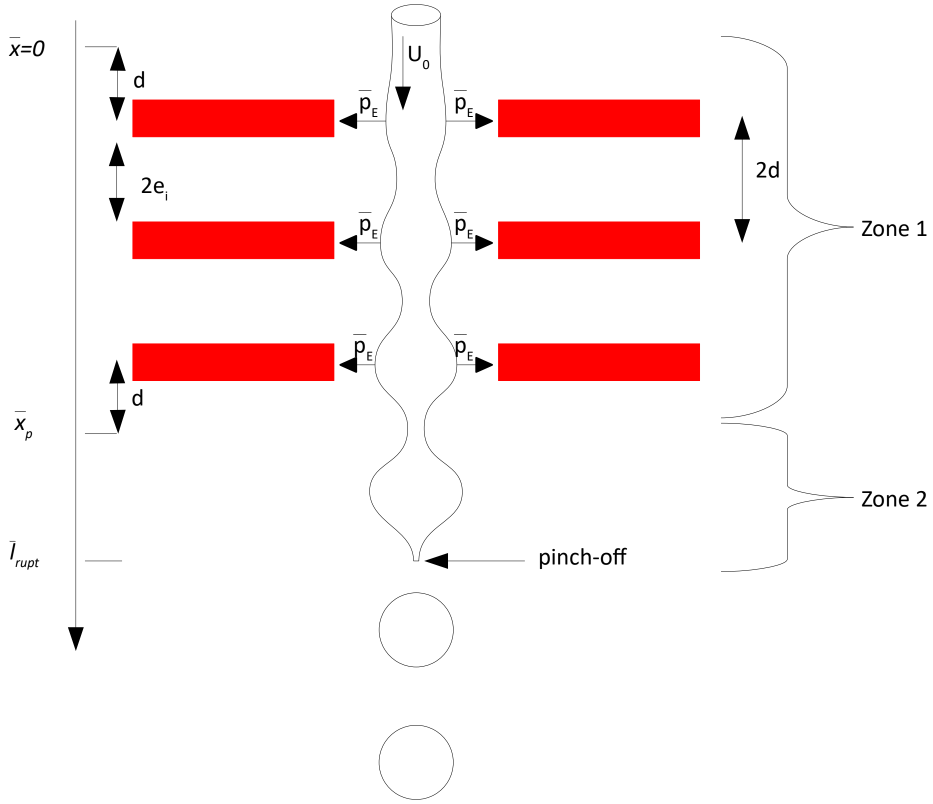

Figure 1. Cross-section of the stacked-type electrofluidic actuator. The circular electrodes are represented by red areas. $\tilde{p}_E$ represents the radially outwards electric stress applied upon the jet interface. Zone 1 is the area where an axial distribution of electric stress is applied. Zone 2 is free of electric stress (no actuation).

A. Mathematical model

One considers a jet of radius $\tilde{R}$ and axial velocity $\tilde{U}$ passing through an area subjected to a radially inwards electric field as depicted in Fig. 1. The electrical conductivity of the liquid phase is assumed to be large enough for the relaxation time of the electric charges to remain much smaller than all other time scales. As a consequence, the whole jet can be supposed to be uniformly grounded.

2-D axial symmetry is supposed for the liquid jet which is described from momentum (1) and mass (2) conservation as well as from the Laplace-Young equation (3), as a simplified form of the normal momentum balance at the jet surface. In a way similar to Lee[44], the mathematical model is simplified by considering the radial velocity to remain much smaller than the axial velocity of the liquid jet (as usual with the slender-jet approximation). By disregarding the viscous force and the body forces, the potential flow can therefore be described first using the axial component of Navier-Stokes equation

$$\frac{\partial \tilde{U}}{\partial \tilde{t}} + \tilde{U} \cdot \frac{\partial \tilde{U}}{\partial \tilde{x}} = \frac{1}{\rho} \cdot \frac{\partial}{\partial \tilde{x}} \cdot (\tilde{p_s} + \tilde{p_e}), \tag{1}$$

where ρ is the density, $\tilde{p}_s$ is the Laplace (over)pressure and $\tilde{p}_e$ is the applied electrostatic stress,

then the continuity equation

$$\frac{\partial \tilde{R}^2}{\partial \tilde{t}} + \frac{\partial}{\partial \tilde{x}} \cdot (\tilde{R}^2 \cdot \tilde{U}) = 0, \tag{2}$$

where $\tilde{R}$ is the instantaneous radial displacement of a point at the surface of the cylindrical jet,

and finally the pressure induced by the curvature of the jet interface,

$$\tilde{p_s} = 2\,T \cdot \kappa, \tag{3}$$

acting as a closure law[1] between the (over)pressure induced by the jet curvature and the mean surface curvature $\kappa(x)$ along the jet, defined as,

$$\kappa = \frac{\dfrac{1}{\tilde{R}} - \dfrac{\partial^2 \tilde{R}/\partial \tilde{x}^2}{1 + (\partial \tilde{R}/\partial \tilde{x})^2}}{2\sqrt{1 + (\partial \tilde{R}/\partial \tilde{x})^2}}, \tag{4}$$

with T, the surface tension.

To linearise at first order the previous equations, it is typically assumed that the radial disturbance, $\tilde{r}$, caused by the application of the electrostatic stress, remains much smaller

---

[1] It is worthy to note that from the kinematic condition (10) written at the deformed jet surface, it is possible to derive the radial velocity and to demonstrate that the normal viscous stress in the jump momentum balance[45] can be usually disregarded since i) the slender-jet assumption is valid ($\tilde{r} \ll R_0$) and ii) the capillary number remains small in the experiments ($Ca = \frac{\tilde{\eta}\tilde{\omega}\tilde{r}}{T} \sim 10^{-2}$, at most, with $\tilde{\eta}$, the Newtonian viscosity and $\tilde{\omega}$, the angular frequency of the disturbance).

than the initial radius of the liquid jet: $\tilde{r} << R_0$, with $\tilde{R} = R_0 + \tilde{r}$. Due to mass conservation, it is also consistent to consider that the velocity disturbance is such that $\tilde{u} << U_0$, with $\tilde{U} = U_0 + \tilde{u}$ and U_0, the mean velocity.

From the linearised forms of the equations (1), (2) et (3), it is possible to establish a unique evolution equation for the radial disturbance $\tilde{r}$:

$$\left(\frac{\partial}{\partial \tilde{t}} + U_0 \cdot \frac{\partial}{\partial \tilde{x}}\right)^2 \cdot \tilde{r} = \frac{-T}{2\rho R_0} \cdot \left[\frac{\partial^2 \tilde{r}}{\partial \tilde{x}^2} + R_0^2 \cdot \frac{\partial^4 \tilde{r}}{\partial \tilde{x}^4}\right] + \frac{R_0}{2\rho} \cdot \frac{\partial^2 \tilde{p}_e}{\partial \tilde{x}^2}\bigg|_{\tilde{R}=R_0} . \tag{5}$$

B. The case of the free capillary jet: brief recalls and notations

The electrical pressure is considered to be zero in this section. We are then brought back to the well-known case of RP instability along a free (inviscid) capillary jet as described by the linear equation (5) but with the last term removed. The solutions of (5) are harmonic and write as :

$$\tilde{r} = \Re\left[a_o . e^{i\left(-\tilde{k}.\tilde{x} + \tilde{\omega}.\tilde{t}\right)}\right], \tag{6}$$

where a_o, $\tilde{k}$ and $\tilde{\omega}$ are the initial disturbance, the wave number and the angular frequency of the disturbance, respectively. By injecting (6) into the previous equation, one obtains a classical dispersion relation for a radial disturbance along a capillary inviscid jet in the linear approach:

$$(2\,We)^{-1} \cdot (\tilde{k}\,R_0)^4 - \left((2\,We)^{-1} + 1\right) \cdot (\tilde{k}\,R_0)^2 + 2\,\frac{\tilde{\omega}\,R_0}{U_0} \cdot (\tilde{k}\,R_0) - \left(\frac{\tilde{\omega}\,R_0}{U_0}\right)^2 = 0, \tag{7}$$

where $We = \frac{\rho\,R_0\,U_0{}^2}{T}$ is the Weber number which represents the competition between inertia and surface tension.

After calculations, the angular frequency can be found to be, $\tilde{\omega} = U_0\,\tilde{k} \pm i \cdot \frac{U_0}{R_0}\,\mu$, with μ, the (non dimensional) growth rate,

$$\mu = (2\,We)^{-0.5} \cdot \tilde{k}\,R_0 \cdot \sqrt{1 - (\tilde{k}\,R_0)^2}, \tag{8}$$

real and positive, provided that the non dimensional wave number $\tilde{k}\,R_0$ ranges between 0 and 1 (only the radial disturbances with a wave number smaller than the inverse of the initial radius are susceptible to grow along the jet). The disturbance $\tilde{r}$ can therefore be written as a linear combination of hyperbolic functions:

$$\tilde{r} = \left[A_1 \cosh\left(\frac{\mu\,U_0\,\tilde{t}}{R_0}\right) + A_2 \sinh\left(\frac{\mu\,U_0}{R_0} \cdot \tilde{t}\right)\right] \cdot \cos\left((\tilde{x} - U_0\,\tilde{t}) \cdot \tilde{k}\right), \tag{9}$$

where A_1 et A_2 are two parameters to be determined from the initial conditions. The radial velocity $\tilde{r}'$ can be calculated from the kinematic condition:

$$\tilde{r}' = \frac{\partial \tilde{r}}{\partial \tilde{t}} + U_0 \frac{\partial \tilde{r}}{\partial \tilde{x}}. \tag{10}$$

By noting the initial disturbance, $\tilde{r}(\tilde{t}=0) = \tilde{r}_0$, as well as the initial normal speed, $\tilde{r}'(\tilde{t} = 0) = \tilde{r}'_0$, the previous parameters are found to be $A_1 = \tilde{r}_0$ and $A_2 = \frac{\tilde{r}'_0 R_0}{\mu U_0}$.

Moreover, as long as $U_0 \tilde{t} >> \frac{R_0}{\mu}$, the expression of the radial disturbance (9) can be greatly simplified:

$$\tilde{r} = \frac{1}{2}\left[\tilde{r}_0 + \frac{R_0 \tilde{r}'_0}{\mu U_0}\right] \cdot \mathrm{e}^{\frac{\mu U_0 \tilde{t}}{R_0}} \cos\left((\tilde{x} - U_0 \tilde{t}) \cdot \tilde{k}\right). \tag{11}$$

The breakup length, $\tilde{l}_{rupt}$, as a measurable data, makes possible the comparison between the model and the experiments. Since it is directly related to the growth rate μ, the breakup length can be modelled by considering a pinch-off condition on the local instantaneous radius, $\tilde{r} + R_0 = 0$, which, by taking into account Eq. (11), delivers the following breakup time:

$$\tilde{t}_{rupt} = \frac{R_0}{\mu U_0} \ln\left(\frac{2 R_0 \mu U_0}{R_0 \tilde{r}'_0 + \tilde{r}_0 \mu U_0}\right). \tag{12}$$

The breakup time $\tilde{t}_{rupt}$ can be related to the breakup length by considering that the radial disturbance is carried by jet inertia at mean velocity U_0 along the axial direction (Taylor hypothesis). From (12), one finally gets:

$$\tilde{l}_{rupt} = \frac{R_0}{\mu} \ln\left(\frac{2 R_0 \mu U_0}{R_0 \tilde{r}'_0 + \tilde{r}_0 \mu U_0}\right), \tag{13}$$

with $\tilde{l}_{rupt} = \tilde{t}_{rupt} \cdot U_0$. Here, $\tilde{r}'_0$ et $\tilde{r}_0$ are still to be determined, which is the ultimate purpose of the following session.

C. The case of the electrified capillary jet

1. Physical phenomenon involved in the destabilisation of an electrified capillary jet

The previous section developed the classical RP instabilities which lead to the breakup of the capillary jet. For the electric free case, the initial surface deformation is neither known, nor controlled. Here we intend to control this initial disturbance by means of an electrostatic pressure, as detailed in sub-section II C 2. By controlling the initial disturbance and especially its wavelength, we could thus control the diameter of the generated drops. At the same time, some other parasite surface deformations could append and generate drops with other diameters. To prevent this from occurring, we want to reduce the breakup length of the jet in order to avoid that parasitic disturbances destabilise the jet. Thus, to favour as much as possible the expected disturbance, one needs the electric stress of a given electrode be as large as possible when the sought capillary disruption passes through the latter. In this study case it concerns the second and the third electrodes, the first one being the one that initiates the surface deformation. So, this corresponds to a certain number of disturbance wavelengths that must be multiples of the inter-electrode distance. Furthermore, considering that the capillary disturbances are convected by the mean flow (Taylor hypothesis) , we conclude that there are singular frequencies of disturbance generation such that the breakup length of the jet is minimised. The following subsections will mathematically develop the condition of minimizing the breakup length as a function of the frequency of the capillary strain induced by the electrostatic pressure and of the inter-electrode spacing.

2. Electrostatic stress

To study the dynamics of the jet in the presence of an electric field, it is necessary to determine the electric stress distribution. The electro-fluidic actuator, briefly discussed in the previous section, is expected to produce a normal component of the electric field in the form of a standing wave. Numerical simulations are performed based on the finite element method in order to solve the Laplace equation for the electric potential in the air gap, between the jet surface and the electrode stack, and hence, to calculate the normal component of the electrostatic field at the liquid surface (see appendix A for details). The simulations are performed over half an electrode gap, here referred to as d, considering the axial periodicity of the electrode stack. To make the simulation as generic as possible, the half spacing between two successive electrodes, d, is also selected as being the length scale and three aspect ratios are defined: $\delta = \dfrac{e_i}{d}$, with e_i the half thickness of the inter-electrode spacing, $\delta_j = \dfrac{R_0}{d}$ and $\delta_g = \dfrac{R_e - R_0}{d}$ where R_e is the radius of an electrode hole. From the numerical simulations, it can be demonstrated that for δ_g large enough, i.e. greater than 0.4, the spatial component of the electric field is well described by a harmonic function along the nearby jet surface, $\tilde{E}(\tilde{x}) = \tilde{E}_{a0} - \tilde{E}_{a1}\,\cos(\tilde{k}^* \cdot \tilde{x})$, where $\tilde{E}_{a0}$ and $\tilde{E}_{a1}$ stand as parameters and $\tilde{k}^*$ is a wave number. In addition, for the stacked-type electro-fluidic actuator presented in this paper, based on a series of electrodes submitted to the same electric potential, it is possible to suppose $\tilde{E}_{a1} \ll \tilde{E}_{a0}$. Finally, the electric field can be considered as being of the form:

$$\tilde{E}(\tilde{x},\tilde{t}) = (\tilde{E}_{a0} - \tilde{E}_{a1}\,\cos(\tilde{k}^*\,\tilde{x})) \cdot \cos(\tilde{\omega}_E\,\tilde{t}), \tag{14}$$

where $\tilde{\omega}_E$ is the angular frequency of the applied electric field.

The electrostatic stress $\tilde{p}_e$ is obtained from the normal projection of the Maxwell tensor at the liquid surface, $\tilde{p}_e(x,t) = \frac{\varepsilon}{2}\,\tilde{E}(\tilde{x},\tilde{t})^2$, with ε, the dielectric permittivity of the air around the liquid jet:

$$\tilde{p}_e(\tilde{x},\tilde{t}) = \frac{\varepsilon}{2}\,\left(\tilde{E}_{a0}^2 - 2\,\tilde{E}_{a0}\,\tilde{E}_{a1}\,cos(\tilde{k}^*\,\tilde{x})\right) \cdot (1 + cos(2\,\tilde{\omega}_E\,t))\,, \tag{15}$$

again considering that $\tilde{E}_{a1} \ll \tilde{E}_{a0}$. Here a steady component arises that is added to an oscillatory component whose frequency is twice that of the voltage signal delivered to the electro-fluidic actuator.

3. Surface deformation

It is interesting to non-dimensionnalize all relevant variables in order to obtain a general solution. In the previous paragraph, we introduced aspect ratios based on d, the half distance between successive electrodes; d is consistently used to non dimensionnalize the differential operators. Table I summarizes the notations for the variables to be considered, their non dimensional counterparts as well as the characteristic scales.

In table I, the dimensionless wavelength related to the electrode stack, $k^* = \pi$ ($\tilde{k}^* = \frac{2\pi}{2d}$), must be distinguished from the dimensionless wavelength related to the interfacial disturbance along the jet, $k = 2\pi\,\frac{d}{\lambda}$. It should also be noted that the angular frequency of the interfacial disturbance, ω, is to be distinguished from the electrical frequency, ω_E. In addition, $\tilde{r}_{01}$ denotes the initial amplitude of the disturbance in zone 1, E_{carac} denotes

Table I.

physical variables	characteristic scales	non dimensional variables
$\tilde{x}$	d	x
$\tilde{r}$	$\tilde{r}_{01}$	r
$\tilde{k}^*$	d^{-1}	k^*
$\tilde{k}$	d^{-1}	k
$\tilde{t}$	$d \cdot U_0^{-1}$	t
$\tilde{\omega}_E$	$U_0 \cdot d^{-1}$	ω_E
$\tilde{\omega}$	$U_0 \cdot d^{-1}$	ω
$\tilde{p}_e$	P_{e0}	p_e
$\tilde{E}_{a0}$	E_{carac}	E_{a0}
$\tilde{E}_{a1}$	E_{carac}	E_{a1}

the characteristic electric field produced by the annular actuator, with $E_{carac} = \frac{\tilde{V}_{max}}{R_0 . \ln(\frac{R_e}{R_0})}$, and finally, P_{e0} is a characteristic scale for the electrostatic stress defined as $P_{e0} = \varepsilon\, E_{carac}^2$. Finally, we can introduce the parameter $L = \frac{2\,d}{\tilde{\lambda}} = \frac{k}{k^*}$ as the ratio between the two previous wavelengths. If the value of this ratio is an integer, one can infer that the electric stress distribution is optimally designed to facilitate the arising of the surface instability provided it is related to the most energetic mode. As already mentioned, two zones can be distinguished each other: one where the electric stress is present and a second one where the jet is free (Fig. 1). It is therefore in zone 1 that the pressure $\tilde{p}_e$ will play a selective role on the nature of the surface disturbance. As already specified in the previous section with the establishment of equation (5), it is therefore necessary to calculate the second derivative of the electrostatic stress:

$$\frac{\partial^2 \tilde{p}_e}{\partial\, \tilde{x}^2} = P_{e0}\, E_{a1}\, E_{a0}\ {\tilde{k}^*}^2\ \cos(\tilde{k}^*\, \tilde{x}) \cdot \Big(1 + cos(2\, \tilde{\omega}_E\, \tilde{t})\Big)\,. \tag{16}$$

The values of E_{a0} et E_{a1} can be found from numerical simulations (appendix A).

From these considerations, the non dimensional form of the evolution equation (5) writes as:

$$\left(\frac{\partial}{\partial t} + \frac{\partial}{\partial x}\right)^2 \cdot r = -\underbrace{\frac{1}{2\,We}}_{i} \cdot \left[\frac{\partial^2 r}{\partial x^2} + {\delta_j}^2 \cdot \frac{\partial^4 r}{\partial x^4}\right] + \underbrace{\frac{Eu_E}{2} \cdot \frac{R_0}{\tilde{r}_{01}}}_{ii} \cdot \left.\frac{\partial^2 p_e}{\partial x^2}\right|_{\tilde{R}=R_0}\,, \tag{17}$$

where $Eu_E = \dfrac{P_{e0}}{\rho {U_0}^2}$ is the electric Euler number.

The newly established equation (17) can still be simplified from a scaling analysis: by considering an electrolyte and standard conditions such as, $U_0 \approx 1 m/s$, $R_0 \approx 10^{-4} m$, $\rho \approx 10^3 kg/m^3$ and $T \approx 10^{-1} N/m$, the Weber number is found to be of unit order: $We \approx O(1)$. For a typical electric field of order 1 kV/mm, the Euler number is also found of unit order: $Eu_E \approx O(1)$. Nevertheless, the term (ii) is proportional to $\dfrac{R_0}{\tilde{r}_{01}}$. To be consistent with the linear approach, it should be recalled that the surface deformation remains negligibly small with respect to the initial jet radius: $\tilde{r}_{01} \ll R_0$ and the capillary term (i) in zone 1 can be disregarded. In view of this, the equation (17) simplifies to:

$$\left(\frac{\partial}{\partial t} + \frac{\partial}{\partial x}\right)^2 \cdot r = \frac{Eu_E}{2} \cdot \frac{R_0}{\tilde{r}_{01}} \cdot \left.\frac{\partial^2 p_e}{\partial x^2}\right|_{\tilde{R}=R_0} . \tag{18}$$

By injecting the expression (16) in equation (18), one finally gets:

$$\begin{aligned}\left(\frac{\partial}{\partial t} + \frac{\partial}{\partial x}\right)^2 \cdot r &= \frac{Eu_E}{2} \cdot \frac{R_0}{\tilde{r}_{01}} \cdot E_{a0}\, E_{a1}\, k^{*2} \cos(k^* x) \cdot (1 + \cos(2\,\omega_E\, t))\,, \\ &= \underbrace{A_1\, k^{*2} \cos(k^* x)}_{[i]} + \underbrace{A_1\, k^{*2} \cos(k^* x) \cdot \cos(2\,\omega_E\, t)}_{[ii]}, \end{aligned} \tag{19}$$

with $A_1 = \dfrac{Eu_E}{2} \dfrac{R_0}{\tilde{r}_{01}} E_{a0}\, E_{a1}$. The non-homogeneous part of eq. (19) is the sum of two forcing terms: a first one, $[i]$, which is stationary, a second one, $[ii]$, which is oscillatory. The equation (19) being linear, the solution can be written as the combination, $r = r_\alpha + r_\beta$, with:

$$\left(\frac{\partial}{\partial t} + \frac{\partial}{\partial x}\right)^2 \cdot r_\alpha = A_1\, k^{*2} \cos(k^* x), \tag{20a}$$

$$\left(\frac{\partial}{\partial t} + \frac{\partial}{\partial x}\right)^2 \cdot r_\beta = A_1\, k^{*2} \cos(k^* x) \cdot \cos(2\,\omega_E\, t). \tag{20b}$$

D. Boundary conditions

The system (20) is valid in the electrically active area (zone 1). To solve it, boundary conditions on the instantaneous radius as well as on the normal velocity at the liquid surface are imposed at the entrance of the actuator:

$$r_i(t, x = 0) = 0, \tag{21a}$$

$$r_i^{'}(t, x = 0) = \frac{\partial\, r_i}{\partial\, t} + \frac{\partial\, r_i}{\partial\, x} = 0, \tag{21b}$$

with i=α, β.

E. Solutions for the radial deformation, r, and the surface velocity, r'

From the boundary conditions, we obtain, all calculations made (appendix B), the following solutions for the two components:

$$r_\alpha(x) = A_1\,\left[1-\cos\left(k^*\,x\right)\right], \tag{22}$$

$$r'_\alpha(x) = A_1\,k^*\sin\left(k^*\,x\right), \tag{23}$$

and

$$\begin{aligned}\hat{r}_\beta(x,t) =& \frac{-A_1}{2\left(L^2-1\right)}\left[\frac{1}{\left(L^2-1\right)}\left(\left(L-1\right)^2 e^{i\,k^*\,(L+1)\,x} + \left(L+1\right)^2 e^{i\,k^*\,(L-1)\,x} - 2\left(L^2+1\right)\right)\right.\\ &\left. - 2\,L\,i\,k^*\,x\right]\cdot e^{i\,(\omega\,t-k\,x)},\end{aligned} \tag{24}$$

$$\hat{r}'_\beta(x,t) = \frac{-i\,A_1}{2\left(L^2-1\right)}\,k^*\,\left[\left(L-1\right)e^{i\,k^*\,(L+1)\,x} + \left(L+1\right)e^{i\,k^*\,(L-1)\,x} - 2\,L\right]\cdot e^{i\,(\omega\,t-k\,x)}, \tag{25}$$

where the notation $\hat{r}_\beta$ refers to as a complex number, a notation which we adopt here without loss of generality insofar as only the amplitude of the disturbance is of interest to us.

F. Breakup length

We now focus on zone 2, i.e. where the jet becomes free again after it has passed throughout the electrofluidic actuator. Under these conditions, one can consider the expression (11) for the development of a radial perturbation along the jet in free conditions,

$$\tilde{r}(x,t) = \frac{1}{2}\left[\tilde{r}_0 + \frac{R_0\,\tilde{r}'_0}{\mu\,U_0}\right]\cdot \mathrm{e}^{\dfrac{\mu\,U_0\,(\tilde{t}-\tilde{t}_p)}{R_0}}\cos\Big(\left(\tilde{x}-U_0\,(\tilde{t}-\tilde{t}_p)\right)\cdot\tilde{k}\Big), \tag{26}$$

with t_p, a phase shift. The latter can be related to the distance between the origin of the frame and the origin of zone 2 by setting $\tilde{x} = U_0\,\tilde{t}$. In other words, if we assume that the electrostatically-induced surface deformation is convected by mean velocity (Taylor hypothesis), the solution for the radial deformation in zone 2 can be rewritten as follows:

$$\tilde{r}(x,t) = \frac{1}{2}\left[\tilde{r}_0 + \frac{R_0\,\tilde{r}'_0}{\mu\,U_0}\right]\cdot \mathrm{e}^{\dfrac{\mu\,(\tilde{x}-\tilde{x}_p)}{R_0}}\cos\Big(\left(U_0\,\tilde{t}-(\tilde{x}-\tilde{x}_p)\right)\cdot\tilde{k}\Big). \tag{27}$$

Here, $\tilde{r}_0'$ and $\tilde{r}_0'$ denote the radial disturbance and the surface velocity at the location $x = x_p$. Their values are still to be determined. To this end, the solutions between the electrically active zone and the free jet zone can be matched based on continuity criteria at $x = x_p$.

First, according to (22) and (23), it can be easily checked that the solutions r_α and r_α' are vanishing at $x = x_p$, knowing that $k^* = \pi$ and that the value of x_p is fixed at 2n due to the spatial periodicity of the actuator ($\tilde{x}_p = 2nd$). As a consequence, the steady contribution of the electric stress does not influence the instability of the jet in zone 2 and the perturbations $\tilde{r}_0$ and $\tilde{r}_0'$ can be estimated from the solutions $\hat{r}_\beta$ and $\hat{r}_\beta'$ at $x = x_p$:

$$\tilde{r}_0 \;\; = \tilde{r}_{01} \cdot |\hat{r}_\beta(x_p)|, \tag{28a}$$

$$\tilde{r}_0' = \tilde{r}_{01} \, \tfrac{U_0}{d} \cdot |\hat{r}_\beta'(x_p)|. \tag{28b}$$

Making use of scaling analysis, it can be demonstrated[8] that the term proportional to r_0' in (27) generally dominates the initial disturbance, $\tilde{r}_0$. Thus the equation (27) is finally written according to the simplified form,

$$\tilde{r}(x,t) = \frac{R_0 \, \tilde{r}_0'}{2 \, \mu \, U_0} \cdot \mathrm{e}^{\dfrac{\mu \, (\tilde{x} - \tilde{x}_p)}{R_0}} \cos\left((U_0 \, \tilde{t} - (\tilde{x} - \tilde{x}_p)) \cdot \tilde{k} \right), \tag{29}$$

with μ, the non-dimensionalised growth rate coefficient, already defined in (8).

So we just have to calculate $\tilde{r}_0'$ from equation (28b). All calculations made (appendix C), one finds:

$$|\hat{r}'(x_p)| = |\hat{r}_\beta'(x_p)| = \frac{2 \, L \, A_1}{|L^2 - 1|} \, \pi \, |\sin(k^* \, L \, n)|, \tag{30}$$

and

$$\tilde{r}_0' = Eu_e \, E_{a0} \, E_{a1} \, \frac{2 \, \pi \, R_0}{\lambda \, |L^2 - 1|} \, |\sin(\pi \, L \, n)|. \tag{31}$$

Finally, the exact expression for the jet length can be obtained from the expression,

$$\frac{\tilde{l}_{2rupt}}{R_0} = \frac{1}{\mu} \ln \left(\frac{2 \sqrt{1 - (\pi \, \delta_j \, L)^2}}{\sqrt{2} \sqrt{We} \, Eu_E \cdot E_{a0} \, E_{a1}} \cdot \frac{|(L^2 - 1)|}{|\sin(\pi \, L \, n)|} \right), \tag{32}$$

Here, $\tilde{l}_{2rupt}$ refers to the coherent length of the free capillary jet[44], i.e. the length of the jet in zone 2, to which the extent of zone 1, namely, $2 \, d \, n$, must be added in order to get the total breakup length $\tilde{l}_{rupt}$.

It is worthy to recall that the breakup length depends on the ratio between the electrode gap and the wavelength of the disturbance: $L = \frac{2 \, d}{\lambda}$. Following Taylor's hypothesis, the angular frequency $\tilde{\omega}_E$ can be considered as inversely proportional to the wavelength of the disturbance. By considering a synchronization frequency $\tilde{\omega}_{Esync}$ associated with the electrode gap (optimal wavelength), the L parameter writes equivalently as $L = \dfrac{\tilde{\omega}_E}{\tilde{\omega}_{Esync}}$. A parameter L larger than $(\pi\,\delta_j)^{-1}$ could not be physically consistent because it would favour a wave number larger than the inverse of the jet radius R_0. Note that the synchronisation frequency is simply defined as:

$$\tilde{\omega}_{Esync} = \frac{\pi\,U_0}{2\,d}. \tag{33}$$

By paying more attention to equation (32), one can see that the L parameter plays a prior role in the influence ratio:

$$\frac{|\sin(\pi\,L\,n)|}{|(L^2-1)|}. \tag{34}$$

When this ratio is maximised, the breakup length is minimised (all other things being equal). The influence ratio is plotted versus the parameter L (Fig. 2) for a number of electrodes $n = 3$ (in agreement with one of our experimental configurations).

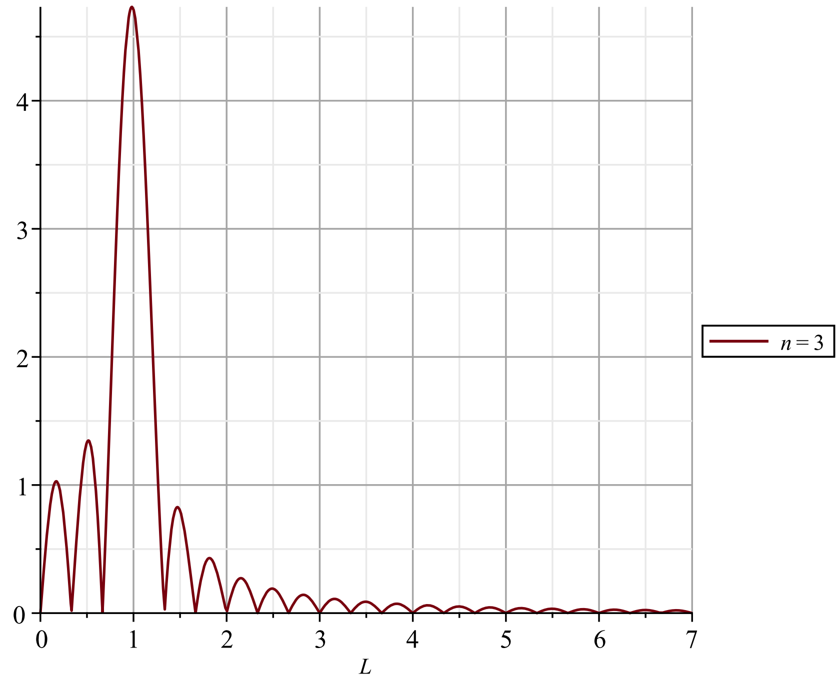

Figure 2. Influence ratio $\frac{|\sin(\pi\,L\,n)|}{|(L^2-1)|}$ as a function of L (number of electrodes: n=3).

From Fig. 2, one first finds that the L parameter maximises the influence ratio (and thus minimises the breakup length) for a discrete set of values which correspond to the ones which maximise the sinus function,

$$|\sin(n\,\pi\,L)| = 1 \Leftrightarrow L = \frac{1}{n}\left(\frac{1}{2}+m\right), m = 0, 1, 2...$$

Note the exception of the overall maximum on the influence ratio, here obtained in L =1, and for which the breakup length may be calculated in the form (appendix C 2),

$$\frac{\tilde{l}_{rupt}}{R_0} = \frac{1}{\mu}\ln\left(\frac{4\sqrt{1-(\pi\,\delta_j)^2}}{\pi\,n\,\sqrt{2}\,\sqrt{We}\,Eu_E \cdot E_{a0}\,E_{a1}}\right). \tag{35}$$

In our approach, the most favourable case corresponds to the smallest breakup length, obtained when the synchronisation frequency favours a wave number as close as possible to the Rayleigh mode, $\tilde{k}\,R_0 = 0.7$ (consider e.g. the marginal stability curve for a capillary jet). One can conclude that the two main parameters of the study, i.e. the signal frequency and the inter-electrode spacing, have two distinct roles. The first one can be set so as to favour discrete frequencies, which depend on the number of electrodes, and in particular on the synchronisation frequency, while the second one allows to fix the wavenumber of the disturbance in relation to the synchronisation frequency.

We are now in a good position for a better interpretation of the experimental results. In particular, the stability model allows us to calculate the natural frequencies expected to minimise the droplet size dispersion.

III. ELECTROFLUIDIC ACTUATION: DESIGN AND EXPERIMENTAL CONDITIONS

A. Experimental device

The experimental device (Fig. 3) is composed of a syringe pump (Genie Kent) to control the flow rate. The syringe containing the liquid under study, a phosphate-buffered saline solution (abbreviated PBS), commonly used in biological research, is then connected to an injector. The latter consists of a rigid copper tube connected to ground and prolonged by an exchangeable rigid plastic nozzle. The inner diameter of the nozzle can range from 0.4mm to 0.52mm and the flow rate supplied can be as high as 30mL/mn. The PBS solution is then injected as a coherent liquid jet passing through a stack of three copper annular electrodes of thickness, e, all connected to the same high-voltage generator. These counter electrodes are separated from each other by spacers which act as electrical insulators and control the inter-electrode spacing, $2\,e_i$. ~~A close-up of the electrofluidic actuator can be seen in Fig. ??~~.

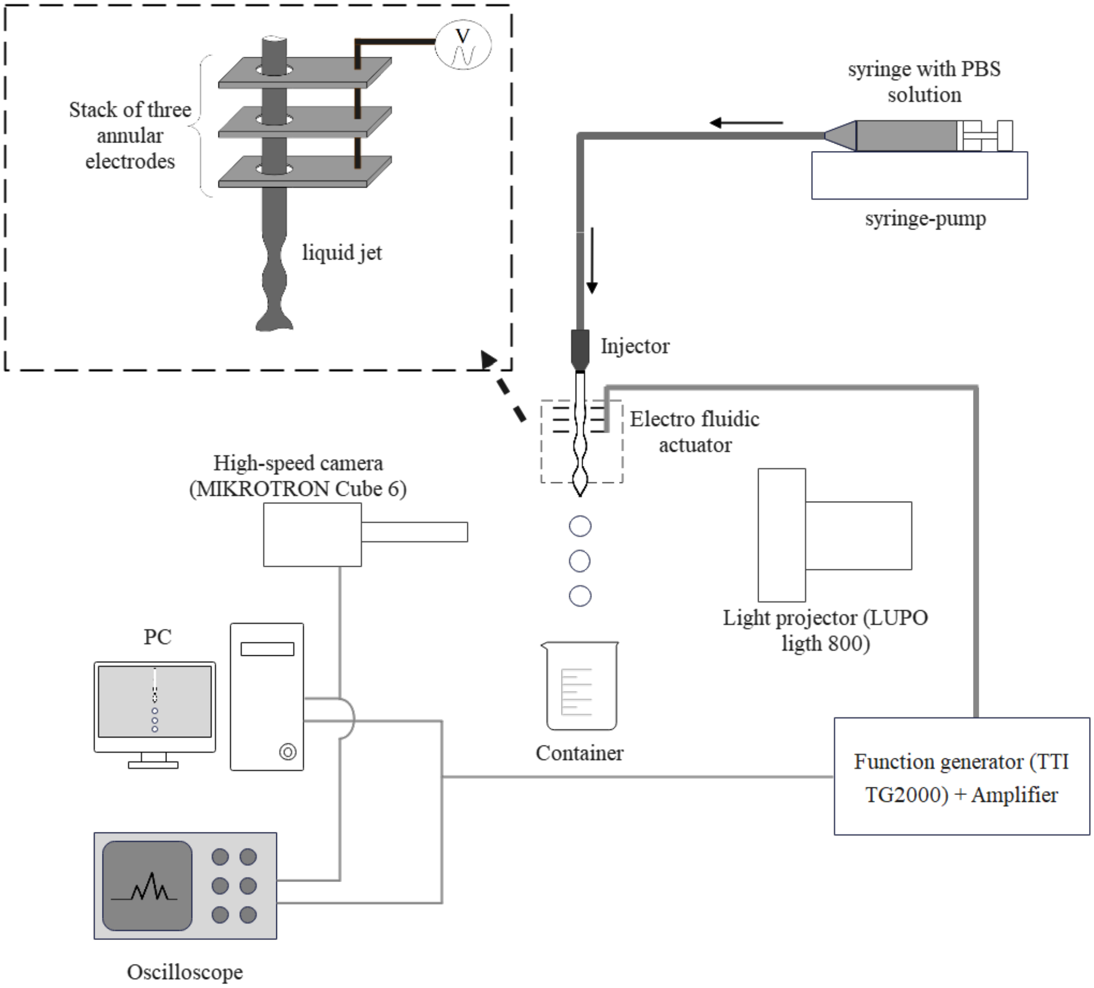

Figure 3. Experimental device. At the top left of the picture, the electric actuator is shown in a close-up view.

The equipment devoted to the generation of an intense electric field consists of a function generator (TTI TG2000) connected to an amplifier (Trek model 20/20C, amplification gain: x2000) and monitored by an oscilloscope (Tektronics TBS1102H). The function generator allows to produce a wide range of harmonic signals with a maximum peak-to-peak amplitude of 20V and a variable frequency. In addition, it can generate a trigger signal useful for the synchronisation between electrostatic actuation and the camera.

The imaging technique used is based on the absorption of light in the pinch-off area where the drops are ejected by atomisation. Use is made of a projector (LUPO light 800) and a diffuser in order to produce an intense but homogeneous light background. Snapshots are taken from a high-speed camera (MIKROTON MotionBLITZ Cube 6) equipped with a long-distance optical zoom. A sequence of images can thus be recorded at up to 2000 frames per second. The camera is triggered by the function generator.

B. Experimental conditions

The PBS solution with a density ρ equal to 1099 kg/m^3 and a surface tension T equal to 77mN/m, is released from the syringe pump at a flow rate, Q. The initial radius and the mean velocity of the jet thus created are denoted respectively R_0 and U_0, where $U_0 = \frac{Q}{\pi\, {R_0}^2}$. Due to the very small relaxation time of PBS solution, $\tau_{relax} = 4\ 10^{-10}$ s, the liquid jet can be considered as uniformly grounded. The liquid jet then passes through the electrostatic actuator. The inner diameter of the ring electrodes is 3.3mm. All of them are connected to the same high voltage $\tilde{V}$, which sustains a radial electric field, $\tilde{E}$, distributed along the surface of the liquid jet. A jump in the normal component of the displacement current at the interface (Gauss's law) induces a surface density of electric charges, which, as a result, counter interacts with the imposed electric field. This two-way interaction is classically responsible for a radially outwards electrostatic stress at the liquid surface.

The electric field can be thought of as a standing wave characterized by an angular frequency, $\tilde{\omega}_E$, and an imposed wave number, $\tilde{k}^*$. The angular frequency is controlled by the user through the function generator while the wave number is governed by the geometry of the electrostatic actuator *via* the thickness to gap ratio of the electrode stack. The choice of the angular frequency allows to favour a particular steady mode for the interfacial disturbance imposed on the liquid jet. The disturbance is then hydrodynamically amplified, even after the jet has left the electrostatic actuator, provided that the dimensionless wave number $\tilde{k}\, R_0$ is smaller than unity. As already mentioned in section II B, after a distance called the breakup length, $\tilde{l}_{rupt}$, the jet self-atomises and drops are ejected. Jet imaging makes it possible to obtain the projected surface of the drops as well as the breakup length of the jet.

Considering that the flow rate, the inter-electrode spacing, the electrode thickness and the initial jet radius are imposed, each test carried out consists of performing a frequency sweep of the applied voltage over a complete duration of 8 seconds. The sweep is performed over the typical range, 100Hz – 550Hz, according to a discrete series of frequency ranges. Each of them is determined from a number of drops high enough to prevent any possible loss of statistical information. Since the camera frequency is 2000 frames per second, the frequency change between two successive snapshots is as small as 30 mHz. During the frequency sweep, the AC voltage is applied as a sinusoidal signal with a peak-to-peak amplitude, $\tilde{V}_{max} = 4$ kV.

IV. METHODS

A. Measurement of the breakup length

Details are given here on the way the breakup length of the jet is extracted from the snapshots issued from the high-speed camera. Image processing consists in thresholding the images in order to obtain binary images. The thresholding is performed following the Otsu's method, which separates the foreground of the image (here the jet and the drops) from the background. In our case the drops and the jet are represented by black pixels, while the background of the image is represented by white pixels (Fig. 4a-4b). Once the thresholding is done, the pixels are summed along one row, considering that: i) one image is made from a discrete series of vertical rows (the gravity and the axis of the jet being supposed horizontal here), ii) black pixels have a unit value and iii) white pixels have a null value. By doing this, one obtains a number density of black pixels as a function of the row (Fig. 4c). From this, one can extract the row associated to pinch-off. Moreover, from the variation of the number density, it is possible to find the respective locations of the nozzle and the electrodes. In the same way, it is possible to locate the drops emitted.

It comes out that it is possible to extract the pinch-off pixel for each image and therefore to determine the breakup length of the jet. Considering that the origin of the liquid jet can be set at the nozzle tip or at the first electrode, all pixel locations can be converted into millimeters. Since the experiments are based on a frequency sweep, each image refers to one frequency of the voltage applied to the electrodes and the breakup length can be given as a function of the frequency.

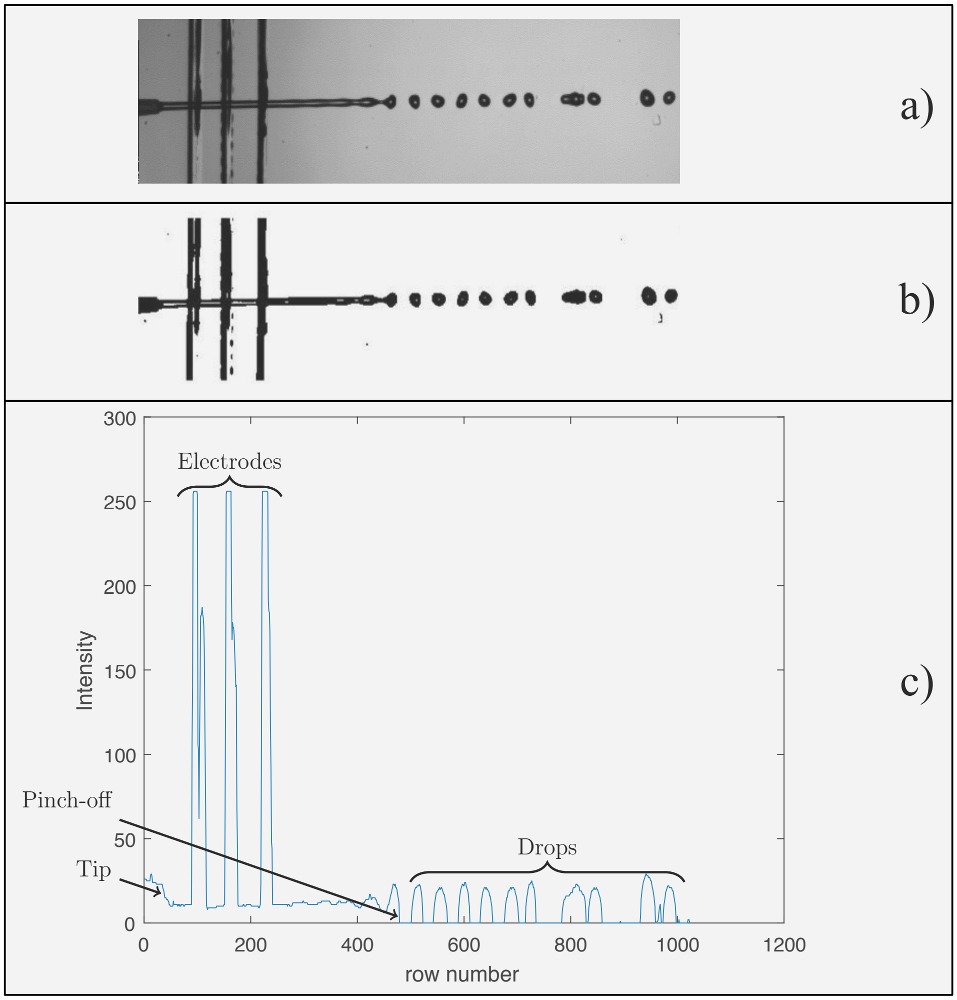

Figure 4. a) Snapshot. b) Image after thresholding by the Otsu method. c) Number density of black pixels.

B. Number of drops required to perform a statistical study

To obtain the particle size distribution, it is necessary to identify the minimum number of drops required for a faithful estimation of the statistical moments. Because it is not possible to obtain the volume of the drops since only one single high-speed camera is used, the statistical study focuses on the projected surface of the drops, i.e. their apparent surface as obtained from the snapshots. The apparent surface is assumed to be constant for each of the drops although this assumption is not totally valid: in fact, just after the atomization step, eventual drop oscillations along the out of plane direction (prolate shape vs. oblate shape) can modify the local measurement of their apparent surface during their fall. To determine the minimum number of drops, a control test is carried out over a sufficiently long period of time. The statistical moments obtained during this test are considered as reference values provided their convergence is achieved. From this, the particle size distribution of the drops is obtained from the apparent surface as extracted. Then, a series of estimates of the particle size distribution is made by decreasing the number of drops analysed. The distributions so obtained are then compared with the reference distribution to obtain a correlation coefficient. Our analysis shows that a minimum number of 865 drops is required to have a correlation coefficient equal to or even better than 0.99.

Beyond this and as already mentioned, a typical experimental test consists in carrying out a frequency sweep for the AC voltage imposed. The latter minimum number of drops therefore imposes a minimum AC frequency range to carry out a statistical estimation faithful to reality, for instance better than 99%. Below 865 drops, the correlation coefficient is experimentally found to drop significantly.

V. EXPERIMENTAL RESULTS

A. Inventory of tests carried out

Two parameters are studied: the radius of the jet and the inter-electrode spacing. Three values of the jet radius are considered: R_0=0.2mm, 0.245mm et 0.26mm. For each of them, three inter-electrode spacings are selected, in order to favour three different wave numbers: the first one close to the wave number maximising the growth rate, *i.e.* $\tilde{k}\,R_0$=0.65 $\sim$ 0.7, a smaller one, $\tilde{k}\,R_0$=0.53, and a larger one, $\tilde{k}\,R_0$=0.76. These wave numbers correspond to the case where the wavelength is equal to the inter-electrode spacing. A synchronisation angular frequency, $\tilde{\omega}_{Esync}$, can be associated with each wave number. $\tilde{\omega}_{Esync}$.

All experimental tests are conducted with a mean velocity of 1.4 m/s, as calculated from the measured flow rate. In addition, a peak-to-peak voltage of 4 kV is applied to the electrodes (electrode thickness: 0.45 mm). By assuming a jet radius of 0.2 mm, the electric Euler number is 5.0×10^{-2} and the Weber number is 5.6. The perturbation of the jet radius due to the electrostatic stress is fairly supposed to be small enough with respect to the gap for the electric field to be considered as externally imposed (weak coupling).

B. Wave number $\tilde{k}\,R_0 = 0.53$

1. Breakup length

This test is carried out under the following conditions: a liquid jet with a radius of 0.2 mm and an inter-electrode spacing of 1.9 mm. The associated synchronisation wavelength is found to be, $\lambda_{sync} = 2.35$mm, which means a non dimensional wave number, $\tilde{k}\,R_0 = 0.53$. Considering the mean velocity of the liquid jet, this wave number suggest an input synchronisation frequency as large as 315Hz so as to get phase lock-in (with $L = 1$, see e.g. modelling section II C).

First, let us compare the experimental breakup length l_{rupt} with the one determined from equation (32). Fig. 5 shows the theoretical and experimental breakup lengths. We can see that the experimental value of l_{rupt} is in fair agreement with the theoretical model, at least in terms of orders of magnitude (few centimeters). Moreover, for a frequency close to 560 Hz, the experimental breakup length increases abruptly, as predicted by the theory as well. Nevertheless, the coherence of the model at low frequencies becomes questionable because of a growing background noise. The latter can be explained by the transient regime generated from sudden application of the actuation voltage. It should also be noted that for the smallest frequencies applied ($\tilde{\omega}_E < 50Hz$), it is not certain that the surface wave electrically induced along the jet interface is still of standing nature (not shown here in Fig. 5b). For the smallest frequencies, it is interesting to notice the presence of a growing jet oscillation travelling downwards (see multimedia view in Fig. 17), similar to a whipping instability[16]. The latter phenomenon is evidently not the object of the present paper since in our strategy, the aim is to favour moderate to high mechanical frequencies. A global trend observed is nevertheless a growth of l_{rupt} for very small frequencies tending to 0 Hz.

As predicted by the theoretical model, peaks are made evident (Fig. 5a) which correspond to local maxima of the breakup length. Referring again to equation (32), these peaks arise when the influence ratio (34) asymptotically tends to zero, i.e. for singular values of L such that $L = \dfrac{1}{n} + m,\ m = 0, 1, 2...,\ L \neq 1$. In the experiments, peaks are significantly damped for $L = \dfrac{1}{3}, \dfrac{2}{3}, \dfrac{4}{3}$ and $\dfrac{5}{3}$ while being discernable for the smallest value $L = \dfrac{1}{3}$ (Fig. 5b). These values of L correspond to resonant frequencies, as theoretically predicted from the model and represented in Fig. 5(a): $\tilde{\omega}_E^{mod} = 103,\ 205,\ 410,\ 513$ Hz. The local maxima of the breakup

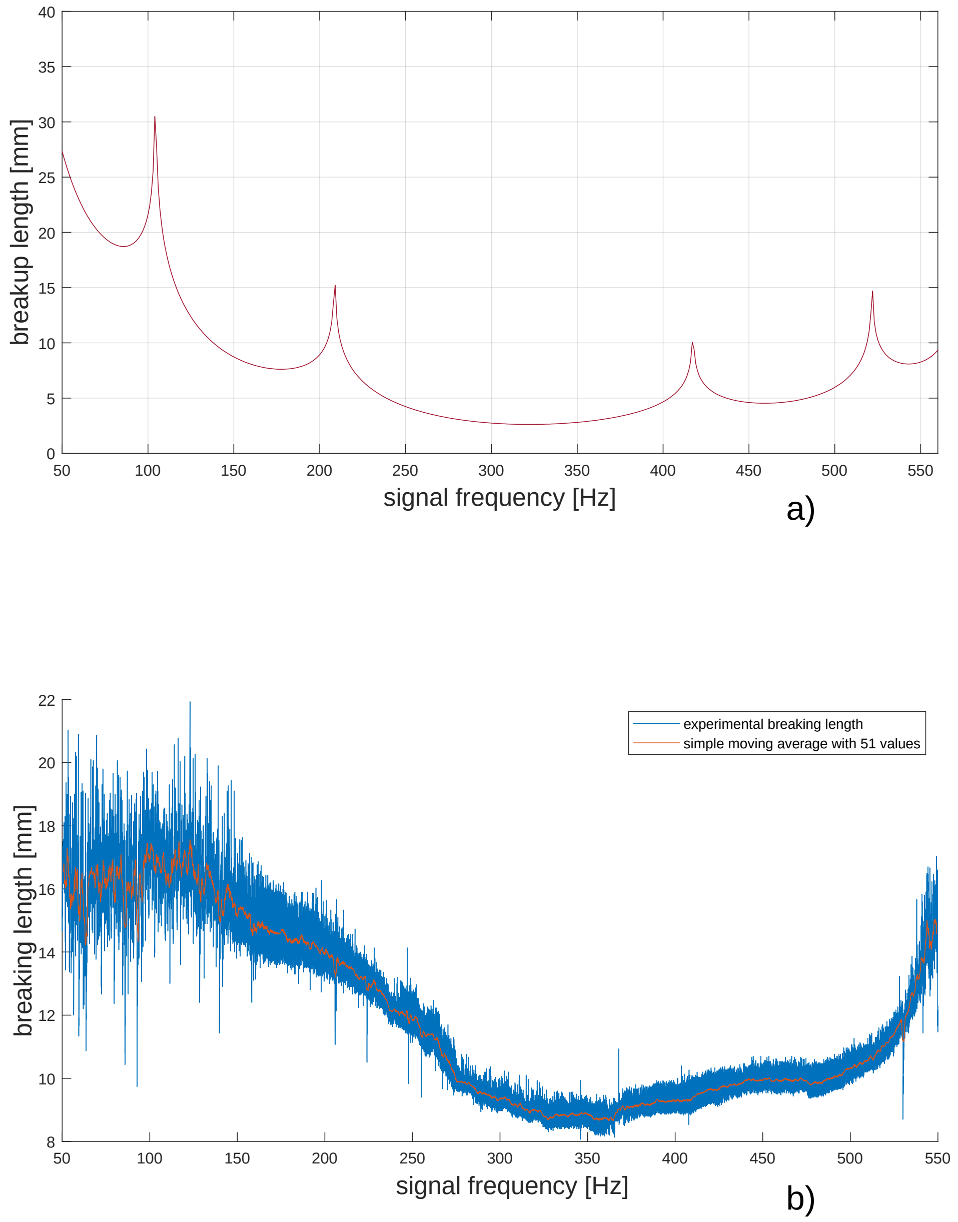

Figure 5. Breakup length as a function of the voltage frequency. (a) Breakup length, as predicted, (b) Breakup length, as measured.

length observed in our experiments are also made evident for experimental frequencies close to those highlighted by the model: $\tilde{\omega}_E^{exp} = 125$ and 200 Hz. Nevertheless, one can notice that for the two last peaks predicted, there is no real experimental counterparts observed.

Another set of experiments has been carried out in order to highlight the impact of the number of electrodes on the breakup length at the synchronization frequency. Table II gives the experimental and theoretical values of the breakup length as a function of the electrode number. As expected by the theoretical model (Eq. 35), the increase in the number of electrodes tends to reduce the breakup length by about 1mm per electrode.

Number of ring electrodes	Experimental values	Theoretical values
1	7.7 mm	5.5 mm
2	6.5 mm	4.2 mm
3	5.3 mm	3.5 mm

Table II. Dependence of the breakup length (as measured in zone # 2 related to the free capillary jet) on the number of ring electrodes. Actuation is set at the synchronization frequency, $\tilde{\omega}_{Esync}$=315Hz.

In an attempt to interpret these findings, two strong assumptions of the model are worth being recalled, which restrict its range of applicability when it is compared with the experimental results. First, the observed breakup length exhibits local maxima that are less pronounced than those predicted by the model. In addition, the observed breakup lengths are slightly longer than their theoretical counterpart. It can therefore be suspected that the viscosity, which is not taken into account in the present model, dampens the frequency peaks (though their values are not changed) and slightly delays jet breakup.

However, the model developed in the previous section remains a robust tool for estimating the actual breakup length of the jet. Robust because despite the fact that the fluid is supposed inviscid, and the fact that non linear effects due to curvature perturbations of the jet are not taken into account, the model delivers fair orders of magnitude and fair values of the resonant frequencies (as it can be checked in the following).

2. Particle size dispersion and determination of resonant frequencies

As explained earlier, a statistical study is devoted to the projected surface of the drops issued from atomization process, i.e. the surface as viewed by the photosensor of the high-speed camera. A frequency sweep is carried out over a delay of 8 seconds. All relevant data available on the snapshots (number of drops and apparent surface) are then processed to obtain a taste of the size distribution from the probability density of the apparent surface area.

A 3-D surface plot is thus obtained based on the probability density of the drop surface area, as calculated on a series of frequency ranges (Fig. 6). The accuracy of the analysis is typically based on these frequency ranges. Most of them can be made evident when the probability density is particularly steep. This corresponds to drops with a particularly low size dispersion. Three relevant statistical moments can be extracted in order to confirm the frequency ranges thus identified: the mean value, the mode[2] and the standard deviation. Fig. 7 represents the evolution of both the standard deviation 7a, and the relative gap from the mean value between the mode and the mean value 7b.

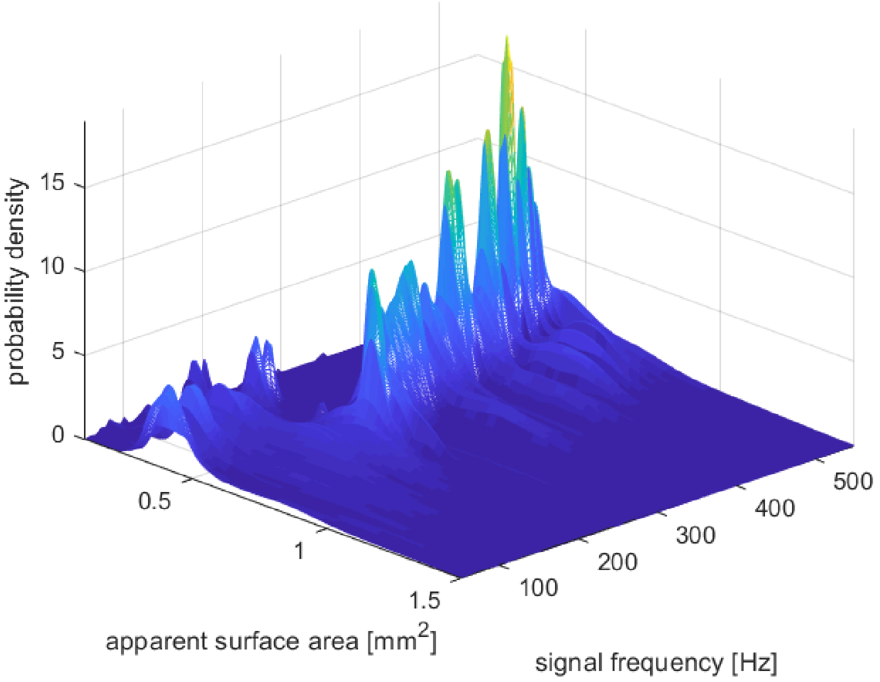

Figure 6. Probability density of the apparent surface area distribution as a function of the voltage frequency (stack of three ring electrodes).

For a frequency range to be reputed relevant for drop-on-demand purposes, the drops produced must exhibit a similar size (mono-dispersed population) with the two following selection requirements: first, the standard deviation, as calculated over a full frequency range, must be minimised as compared to its global evolution, and second, the calculated mode

---

[2] The mode is defined here as the apparent surface area which is the most often represented in the surface area distribution

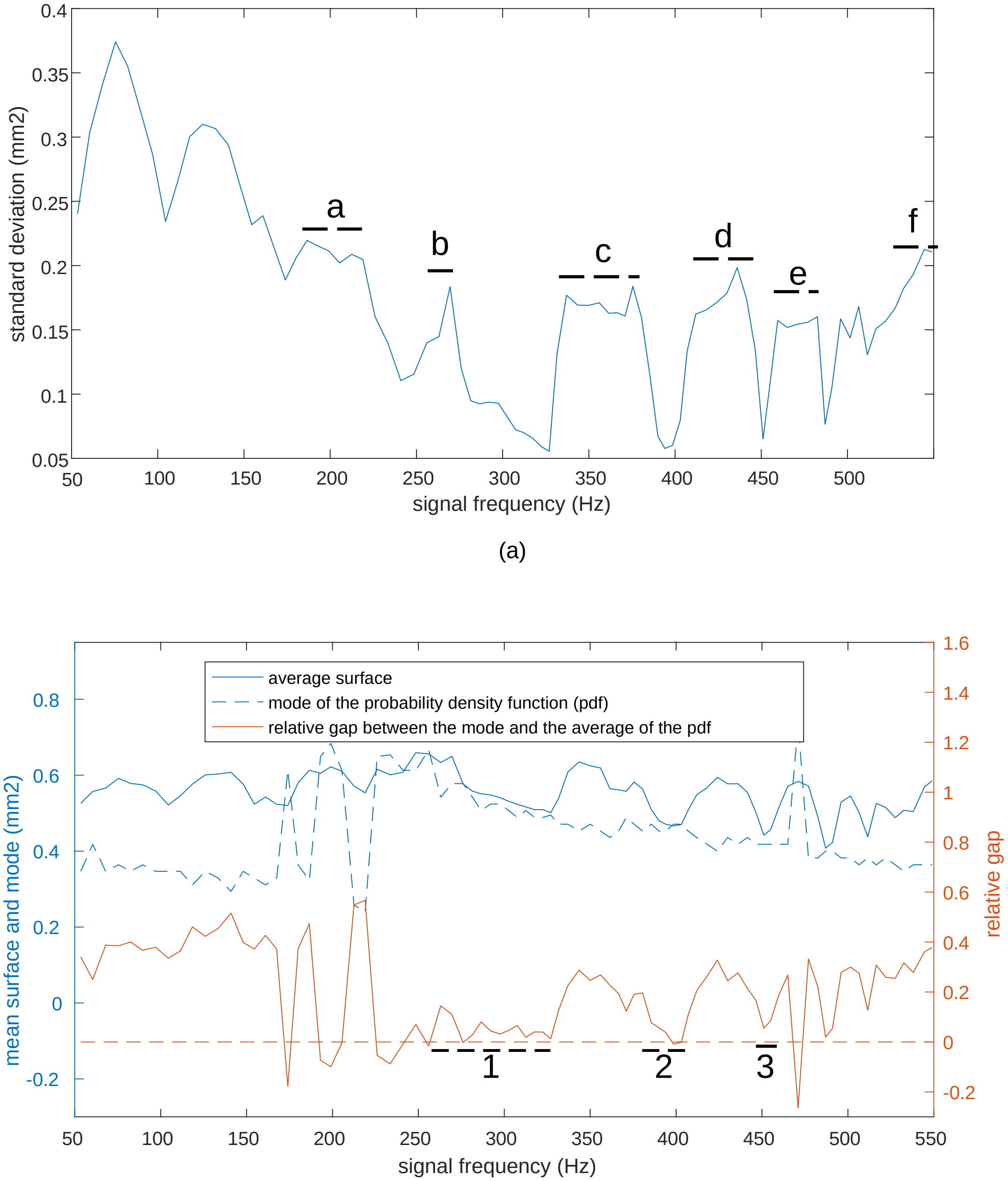

(a)

(b)

Figure 7. Statistical moments as calculated from the probability density. (a) Standard deviation. (b) Mean value, mode value and relative gap between mean and mode values. The frequency ranges characterising a high standard deviation are presented by dotted segments labelled a-f. The segments labelled 1-3 represent the frequency ranges where monodiperse drops are observed.

must be as close as possible to the mean value. The first criterion is relatively straightforward: since a small dispersion of the drop sizes is required, it is consistent to minimise the standard deviation. The second criterion is a little more tricky. A frequency range, said to be of interest, must favour one particular apparent surface area. However, it is possible to obtain a small standard deviation without selecting one single drop size. The simplest example to illustrate this is the presence of two mode values that remain near each other: in such a case, the standard deviation can reveal itself to be small while two distinct sizes can be mostly represented, typically in presence of satellite drops. The second criterion eliminates this kind of situation because it requires that the most represented value, i.e. the mode value, be as close as possible to the mean value.

Thus, according to Fig. 7, one can note the presence of three frequency ranges which meet the two criteria outlined above, the first one located between 300 and 330 Hz (frequency range # 1), the second one between 385 and 405 Hz (frequency range # 2) and the third one between 445 and 455 Hz((frequency range # 3). Appendix D provides snapshots for different frequencies. One can note that one synchronisation frequency, $\tilde{\omega}_{Esync}$=315 Hz, is found to be properly centred within the first frequency range. As expected, the electrostatic actuator favours the arising of surface disturbances with a wave number $\tilde{k}\,R_0 = 0.53$. Moreover, one can notice that the mean surface area of the drops decreases with the actuation frequency. This is consistently explained by the fact that a higher input frequency favours a surface disturbance with a smaller wavelength. Assuming that the volume of the drops produced is proportional to the wavelength of the perturbation[3], it comes out that a growing frequency of the actuation signal induces smaller drops (or equivalently a smaller apparent surface area of the drops).

The theoretical model, and more particularly the influence ratio (Eq. 34), provides us with a series of frequencies for which the breakup length is significantly shortened, and a series of frequencies for which it is significantly extended. Fig. 8 illustrates the comparison between these frequencies and the frequency ranges as experimentally obtained. In Fig. 8a, the frequency ranges of interest are characterised by a small standard deviation and a small relative gap between the mode and the mean value (table III). Its worthy to note that not all of them are associated with a theoretical frequency (370 Hz and 460 Hz respectively).

---

[3] This statement is based on mass conservation: assuming that the volume V_g of an ejected drop is approximated by the volume of a cylinder whose radius is R_0 (radius of the jet) and height is λ (the wavelength of the excited surface disturbance), the following estimate $V_g \sim \frac{3}{4}\,R_0^2\,\lambda$ can be proposed.

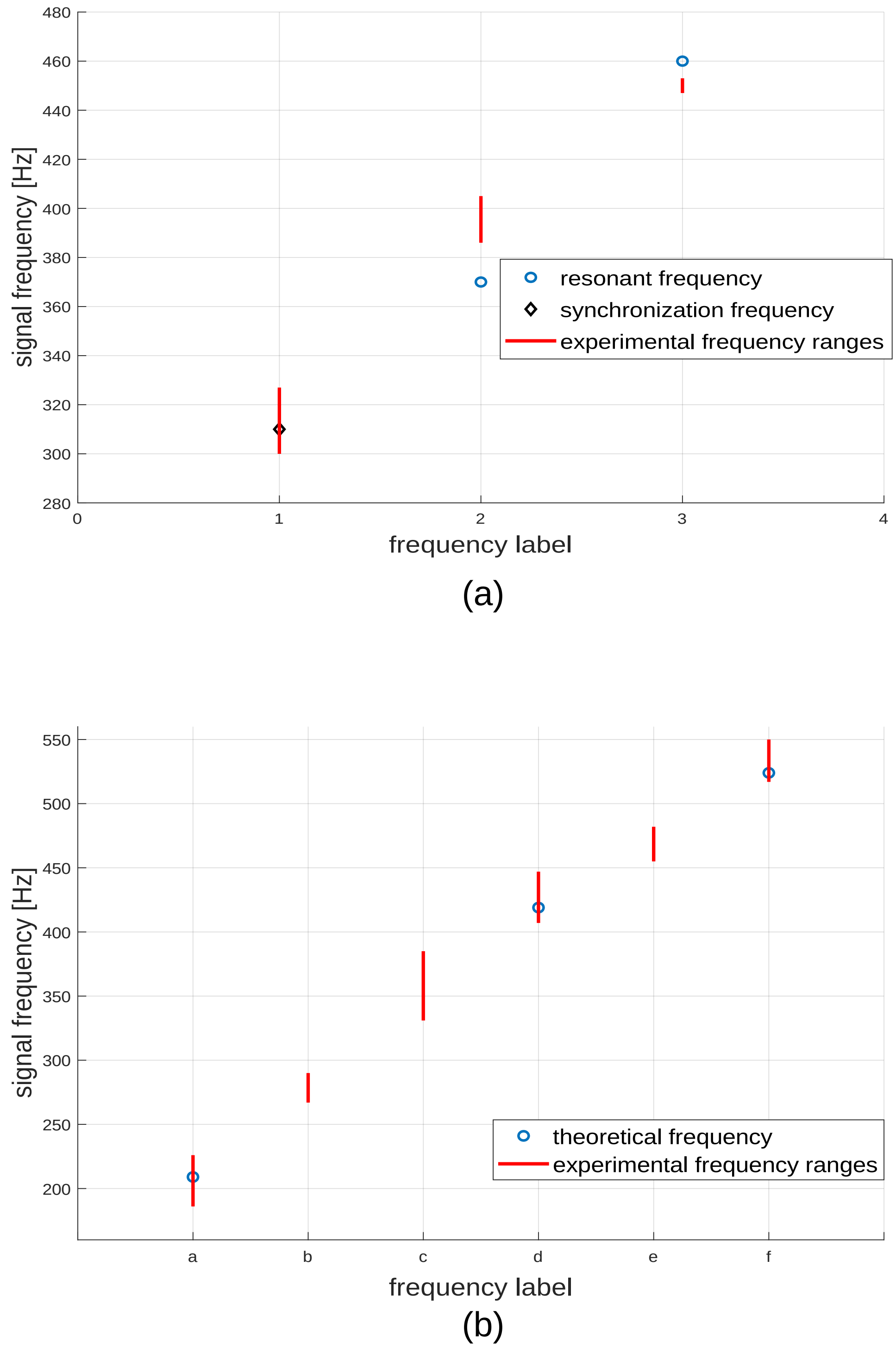

Figure 8. (a) Theoretical frequencies maximising the influence ratio with frequency ranges characterised by a small standard deviation. (b) Theoretical frequencies minimising the influence ratio and frequency ranges in accordance with Fig. 7 characterised by a high standard deviation.

Nevertheless, the synchronisation frequency ($\tilde{\omega}_{Esync} = 315$Hz) is consistently found right in the first frequency range. Fig. 8b gives the experimental frequency ranges characterised by a high standard deviation, as already noticed in Fig. 7a, together with associated theoretical frequencies which minimise the influence ratio.

frequency range	Lower bound	Upper bound
1	292 Hz	327 Hz
2	386 Hz	405 Hz
3	447 Hz	453 Hz

Table III. Lower and upper bounds of the frequency ranges in favour with a monodispersed spray.

Complementary colormaps are plotted in order to investigate the electrodynamic actuator ~~electrospray~~, based on two parameters. The first one is the hydraulic diameter, D_{21}, defined as, $\dfrac{4\,S}{P}$, where S is the apparent surface of the drop and P is the perimeter. One can note that if one drop is found purely spherical, its hydraulic diameter equals its disk diameter, D_{20}, here defined as, $D_{20} = \sqrt{\dfrac{4\,S}{\pi}}$.
The drop size distribution is plotted, based on the dimensionless ratio of the hydraulic diameter D_{21} to the diameter of the jet (Fig. 9). Not surprisingly, the frequency ranges characterised by a low dispersion are recovered beyond a cutting frequency as large as 215Hz. In light of Fig. 9, the diameter D_{21} is found to be between 1.6 and 2.2 times the jet diameter. Here, the red dash line corresponds to a normalised diameter as anticipated by considering a disturbance wavelength equal to the gap between two successive electrodes. This synchronization hydraulic diameter is calculated considering a volume of drop which linearly depends on the disturbance wavelength (as explained above). The drop size distribution is therefore found consistent with the latter synchronization diameter as obtained for the synchronization frequency, $\tilde{\omega}_{Esync} = 315$Hz. Moreover, still regarding Fig. 9, the diameter ratio exhibits a linear dependence on the signal frequency, which also supports the fact that the drop volume is proportional to the disturbance wavelength.

On Fig. 10 is plotted the distribution of the ratio of the hydraulic diameter to the disk diameter, as a function of the actuation frequency. This stands as an indicator of the discrepancy from a spherical shape, as a result of drop deformation due to shape oscillations for instance. Here, especially in the frequency ranges that favour a mono-dispersed stream,

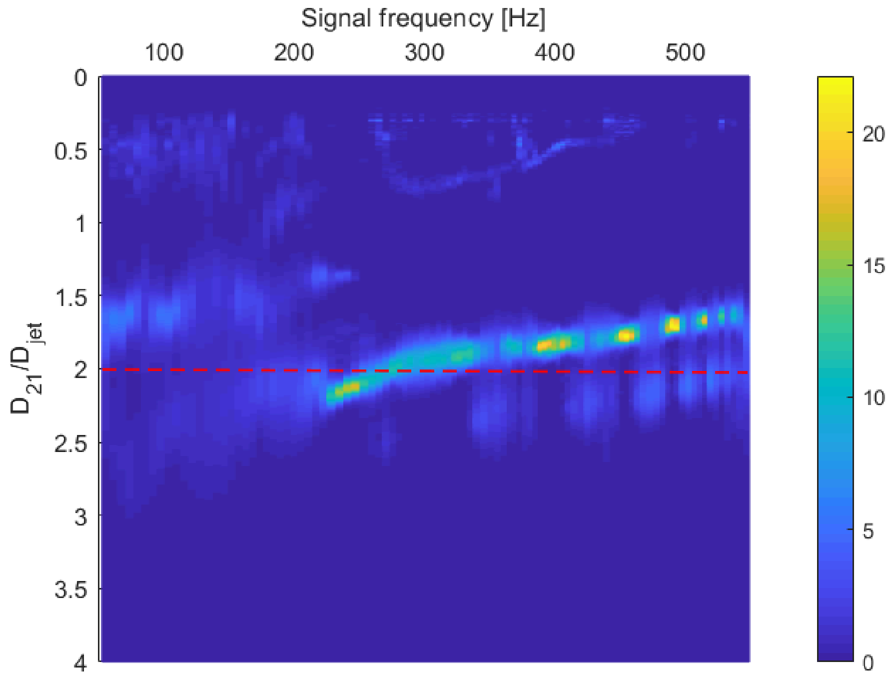

Figure 9. Probability density of the normalised diameter, D_{21}/D_{jet}, as a function of the actuation frequency ($D_{jet} = 2R_0$). The red dash line represents the diameter ratio as calculated from a disturbance wavelength supposed to be equal to the electrode gap ($\lambda = 2d$). Data obtained with a stack of three electrodes.

it can be checked that this diameter ratio remains close to unit, together with a reduced dispersion and therefore a negligible coalescence of unequal sized drops.

Complementary experiments are also performed in the same conditions as before but for a variable number of electrodes (n=1, 2, 3, see Fig. 11). The impact of the electrode number on the surface area distribution is investigated for a large range of the actuation frequency. A larger number of electrodes tends to amplify the probability density for the high resonant frequencies, which is consistent with theoretical expectations. However, as shown in Table IV, resonant frequencies related to the peaks slightly move with the electrode number. For instance, the peak [1a] does not display the exact same frequency as those related to peaks [2a] and [3a]. Finally, whatever the number of electrodes, there always exists a rather large frequency range for which a population of drops with a tightened size distribution can be associated. In Fig. 9, these frequency ranges typically fit into an interval delimited by text-boxes labelled *na* and *nb* (n=1, 2, 3).

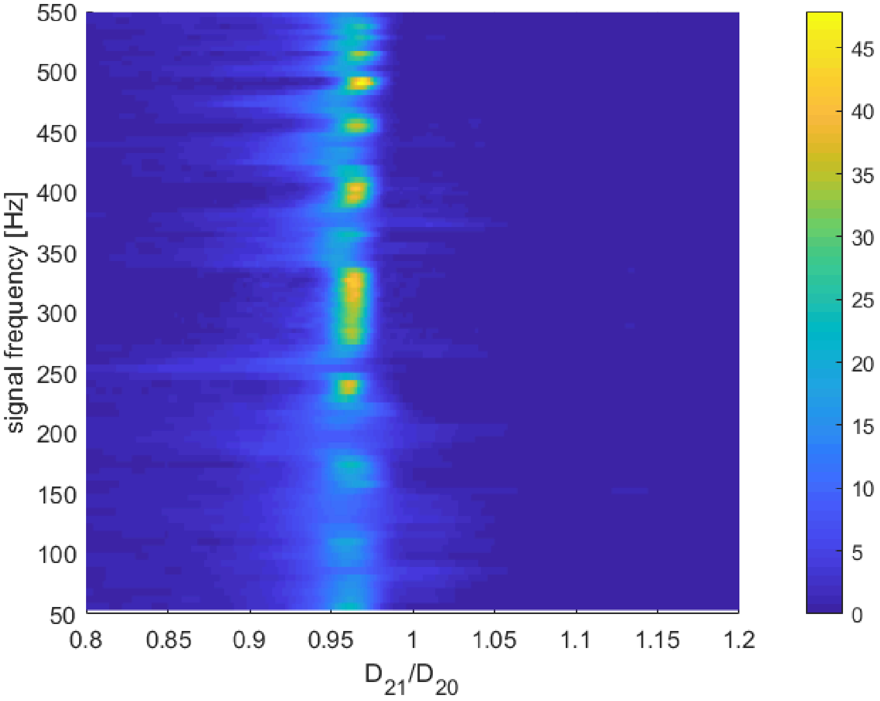

Figure 10. Probability density of the normalised diameter, D_{21}/D_{20}, as a function of the voltage frequency. Data obtained with a stack of three electrodes.

The orders of magnitude provided by the model including the breakup lengths estimated for asymptotic frequencies (i.e. for frequencies tending towards 0Hz and 560Hz) are consistent with the observations. Moreover, some of the maximum values for the breakup length, as predicted by the theory, find their counterparts in the post-processed data, albeit with a much smaller value of the breakup length and with associated frequencies that can differ slightly. Of course, these discrepancies can be explained by unavoidable experimental uncertainties on the inter-electrode spacing, the electrode thickness or the jet radius for instance, but some physical mechanisms are also disregarded (viscous damping, non linear jet deformation).

Despite these limitations, the methodology proposed demonstrates its ability to deliver a series of frequencies in favour with a monodisperse spray of drops, including the synchronisation frequencies, but also its ability to provide unfavourable frequencies, i.e. frequencies that locally maximise the particle size dispersion of the drops.

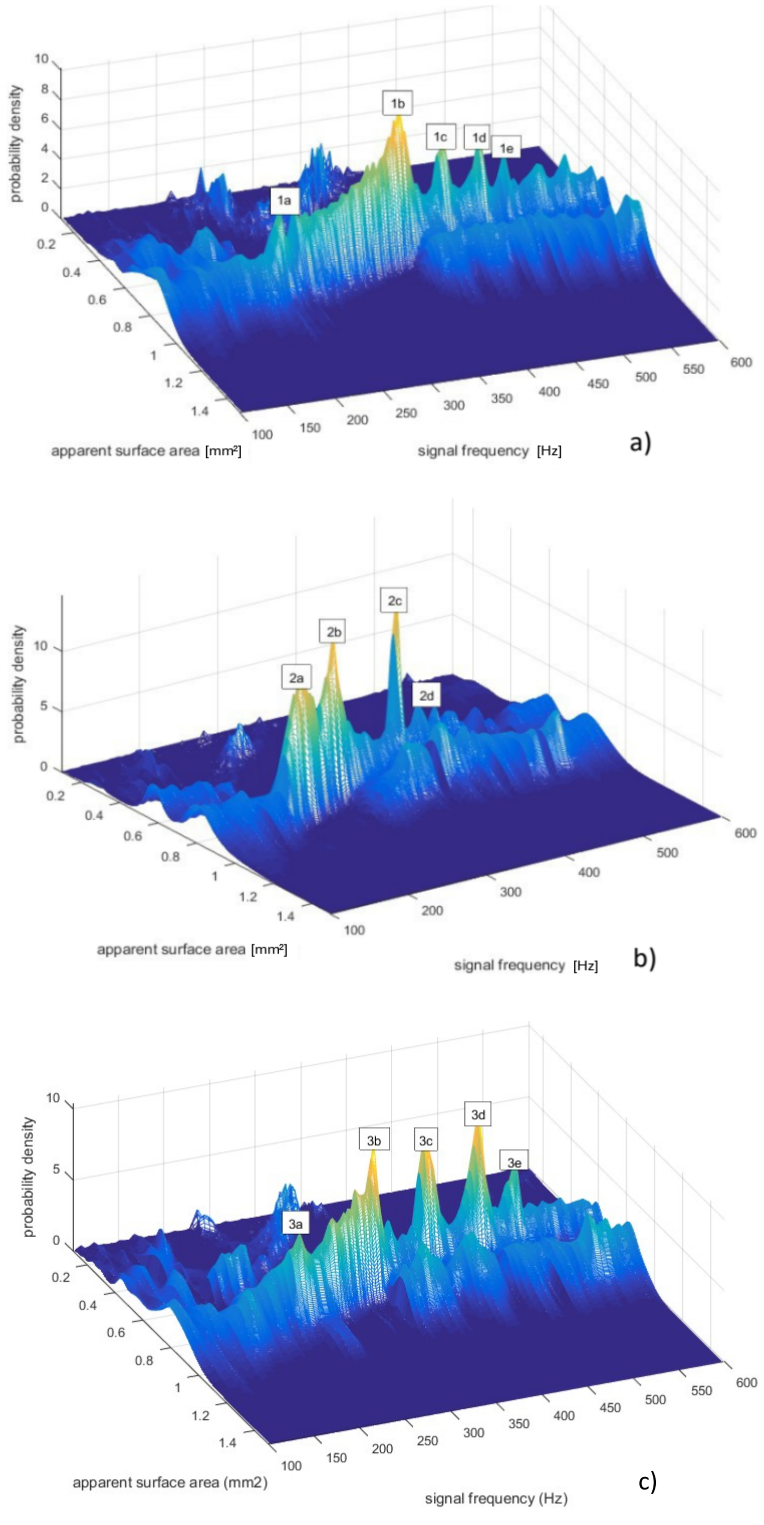

Figure 11. Probability density of the apparent surface area distribution for a growing number of actuation electrodes, a) one single electrode, b) an electrode pair, c) a stack of three electrodes. Frequencies of interest are made visible from labelled text-boxes (see also Table IV).

one electrode		two electrodes		three electrodes	
Name	Frequency	Name	Frequency	Name	Frequency
1a	251 Hz	2a	212 Hz	3a	240 Hz
1b	375 Hz	2b	282 Hz	3b	339 Hz
1c	428 Hz	2c	390 Hz	3c	400 Hz
1d	465 Hz	2d	422 Hz	3d	465 Hz
1e	493 Hz			3e	505 Hz

Table IV. Actuation frequency related to peaks labelled as text boxes displayed in Fig. 11.

C. Key results obtained with $\tilde{k}\,R_0 = \{0.53,\ 0.65,\ 0.76\}$

All experimental results obtained with the previous methodology for different wave numbers can be summarised in order to get an overview of the efficiency of the electrostatic actuator. To this end, three tests are carried out with a variable inter-electrode spacing, a constant flow rate and a constant jet radius (R_0=0.2mm). For this first series of tests, the Weber number is given fixed, equal to 5.9. To each inter-electrode spacing, and given the flow rate, it is possible to associate a wave number $\tilde{k}\,R_0$ in favour with lock-in (synchronised) atomisation. The wave numbers selected are: $\tilde{k}\,R_0$={0.53, 0.65 and 0.76}. Figures 12(a) and 12(b) illustrate the frequency ranges of interest and the frequencies theoretically determined as a function of the wave numbers investigated.

In view of these results, it is worthy to note that the synchronisation frequency is not observed for all the frequency ranges experimentally tested. This is especially true when the wave number tends to 1, which can be explained by the fact that it is more difficult to favour short wavelength perturbations. Indeed, in free regime, when the wavelength of the disturbance tends towards the radius of the jet, its growth rate is strongly reduced as a consequence of the marginal stability curve. Also, when the desired wave number $\tilde{k}\,R_0$ is close to 1, the resonant frequencies actually favoured are smaller than the synchronisation frequency. We can conclude that it is easier to favour wavelengths longer than the jet radius. Moreover, for each wave number, the theoretical model delivers at least one resonant frequency producing homogeneous drops, this frequency being always smaller than or equal

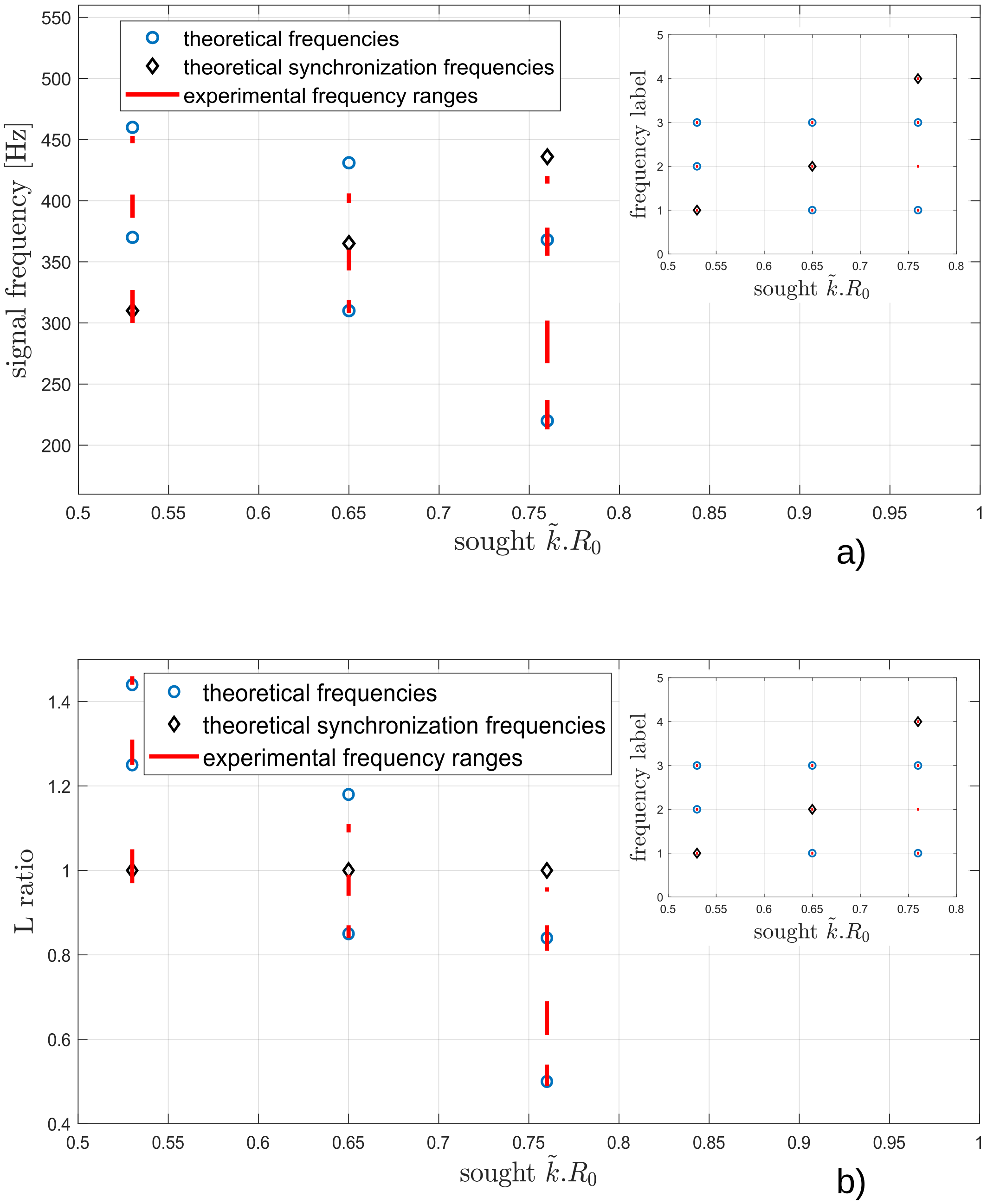

Figure 12. Frequency ranges under consideration and theoretical frequencies (resonant and synchronisation ones) as a function of the experimental wave number (kR_o={0.53, 0.65, 0.76}): (a) Dimensional values of the frequencies, (b) Same frequencies normalised by the synchronisation frequencies as calculated for each wave number. Inserts: frequency labels are sorted from the lowest frequency to the highest one, for a given value of sought kR_o.

to the synchronisation frequency.

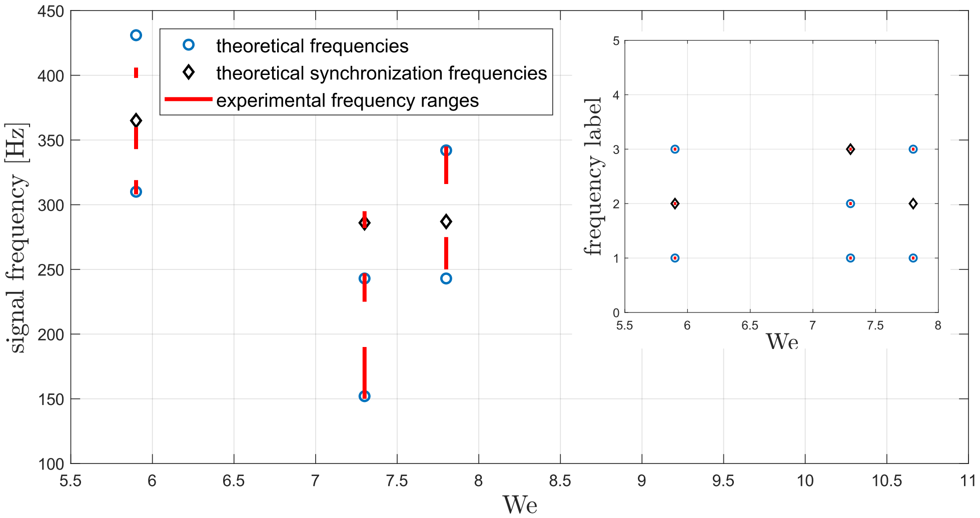

Figure 13. Frequency ranges of interest (small drop size dispersion) and theoretical frequencies as a function of the Weber number: We = [5.9, 7.3, 7.8]. Insert: for a given Weber number, frequency labels are sorted from the lowest frequency to the highest one.

A second series of tests is conducted to investigate the influence of the Weber number on the frequency ranges of interest, especially the ones for which one can obtain a weak drop size dispersion. These tests are carried out with different jet radii (R_o = 0.2, 0.24 et 0.26 mm), a constant flow velocity (1.4m/s) and a constant wave number: k^*=0.65. A variation of the jet radius allows, all other things being equal, to modify the Weber number, We. Fig. 13 illustrates a rather weak We-dependence of the frequency ranges associated to a small drop size dispersion. This is consistent with the fact that the influence ratio (34) is not modified. One recalls that the Weber number was made to change during the experiments by adjusting the jet radius rather than the flow rate. It was therefore necessary to adjust the electrode gap in order to keep the desired wave number as close as possible to the target value, $k^* = 0.65$. Due to practical limitations, one series of tests was nevertheless conducted with the wave number, $k^* = 0.69$. It is also worthy to recall that the Weber number still governs the breakup length due to the growing influence of inertia with the impact of the growth rate upon surface waves delayed downstream.

VI. FINAL DISCUSSION

Electrostatically-assisted atomisation in jetting regime ranks among good options for digital applications which require monodispersity of droplets between hundreds of micrometers and millimetre range together with a throughput higher than the one achievable in dripping or cone-jet regimes.

The actuator studied in this article is based on the use of electrostatics in order to generate the parametric instability of a capillary liquid jet and its subsequent atomisation. The originality of the approach proposed consists in forcing a stationary mode by making use of a periodic stacking of electrodes. The objective is then to study the role of the inter-electrode spacing. The experiments carried out demonstrate a decisive influence of this spacing on the frequency of the signal to be applied in order to obtain a train of monodispersed drops with a fixed size. Indeed, based on a theoretical model developed in support, it is shown that the inter-electrode spacing makes it possible to force a series of surface perturbation modes, in particular the modes calculated from the inter-electrode spacing and the thickness of the electrodes. At a given flow rate, the frequency can be monitored so as to generate the most unstable mode which favours the jet breakup. Among the resonant frequencies, some belong to frequency ranges, said of interest due to the very small standard deviation observed on the subsequent drop size distribution. These particular frequencies, here referred to as synchronisation frequencies (lock-in frequencies), are identified experimentally. Not only they favour the jet breakup but they also promote a monodispersed dispense of drops with interesting perspectives for drop-on-demand applications.

The stacked-type electro-fluidic actuator here proposed therefore stands as a good option to produce a monodisperse spray. The frequencies of the voltage signal to be applied can be predicted by means of a model integrating the device parameters (inter-electrode spacing, flow rate, electric field, fluid properties).

It must be noted however that in our study, model predictions are not systematically in perfect agreement with experimental results. This can be explained by the assumptions related to the 1-D linear model proposed (inviscid fluid, Taylor hypothesis, uniform axial velocity for instance) as well as by the geometrical uncertainties related to the experimental device such as the difficulty to lign up the stack of pierced electrodes with the axis of the capillary jet.

The present study is focused on one particular strategy, the electrostatic forcing of an oscillatory capillary wave with subsequent shaping of the liquid jet. Optimisation paths can be considered later on. Two of them are fully compatible with our system and consist in further optimising the actuation signal and the shape of the electrode edges.

ACKNOWLEDGMENTS

Special thanks are due to Jean-Paul Baroux and Jean-Luc Reboud (G2Elab laboratory, Grenoble, France) for the last-minute loan of an amplifier (TREK 20/20C). Their help was especially decisive when our own amplifier failed. Francois Bonnel must also be acknowledged for his helpful assistance. The laboratory SIMaP is part of the LabEx Tec 21 (Investissements d'Avenir – Grant Agreement No. ANR-11-LABX-0030).

Appendix A: Calculation of the electric field, as produced by the electric actuator

The electric field is calculated in the air gap between the jet and the electrodes in order to obtain the distribution of the normal electric stress along the liquid jet and therefore to verify that the assumption of a harmonic distribution for the electric stress remains robust. The liquid jet is supposed not to be significantly deformed so that the problem can still be considered as 2D-axisymmetric. Axial periodicity is supposed due to electrode stacking (Fig. 14a). The aspect ratios, $\delta = \frac{e_i}{d}$, $\delta_j = \frac{R_0}{d}$, $\delta_g = \frac{R_e - R_0}{d}$, are introduced, with d, the half-distance between two successive electrodes, e_i, the half-thickness of one electrode, R_e, the radius of the electrode hole, R_0, the radius of the liquid jet. Finite element method is used to solve the non-dimensional form of the Laplace equation in cylindrical coordinates,

$$\frac{\partial^2 \phi}{\partial r^2} + \frac{1}{r}\frac{\partial \phi}{\partial r} + \frac{\partial^2 \phi}{\partial x^2} = 0,$$

taking into account the following boundary conditions (Fig. 14a):

$$V(r = \delta_j, x) = 0 \tag{A1}$$

$$V(r = \delta_j + \delta_g, x) = 1 \; for \; x \; \geq \; (1 - \delta) \tag{A2}$$

$$\frac{\partial V}{\partial r}(r = \delta_j + \delta_g, x) = 0 \; for \; x \; \leq \; (1 - \delta) \tag{A3}$$

$$\frac{\partial V}{\partial x}(x = 0) = 0 \; for \; \delta_j \leq \; r \; \leq \; (\delta_j + \delta_g) \tag{A4}$$

$$\frac{\partial V}{\partial x}(x = 1) = 0 \; for \; \delta_j \leq \; r \; \leq \; (\delta_j + \delta_g) \tag{A5}$$

Parametric simulations are performed for different values of δ, δ_j and δ_g. The numerical results are post-processed under Matlab. As illustrated by Fig. 15b, the (tangent) x-component of the electric field along the liquid jet remains vanishingly small provided that δ_g is large enough with respect to δ. As a consequence, the normal component of the electric field at the surface of the liquid jet is the relevant variable to be fitted for instance from two Fourier modes:

$$E_{n,s} = E_{a0} + E_{a1}\, cos(k\,x) + E_{b1}\, sin(k\,x) + E_{a2}\, cos(2\,k\,x) + E_{b2}\, sin(2\,k\,x) \tag{A6}$$

Here, use is made of the expression, $E_{carac} = \frac{V_{max}}{R_0 \ln(\frac{R_e}{R_0})}$, as a characteristic scale to normalise the electric field accross the air gap. The latter is considered as an annular capacitor

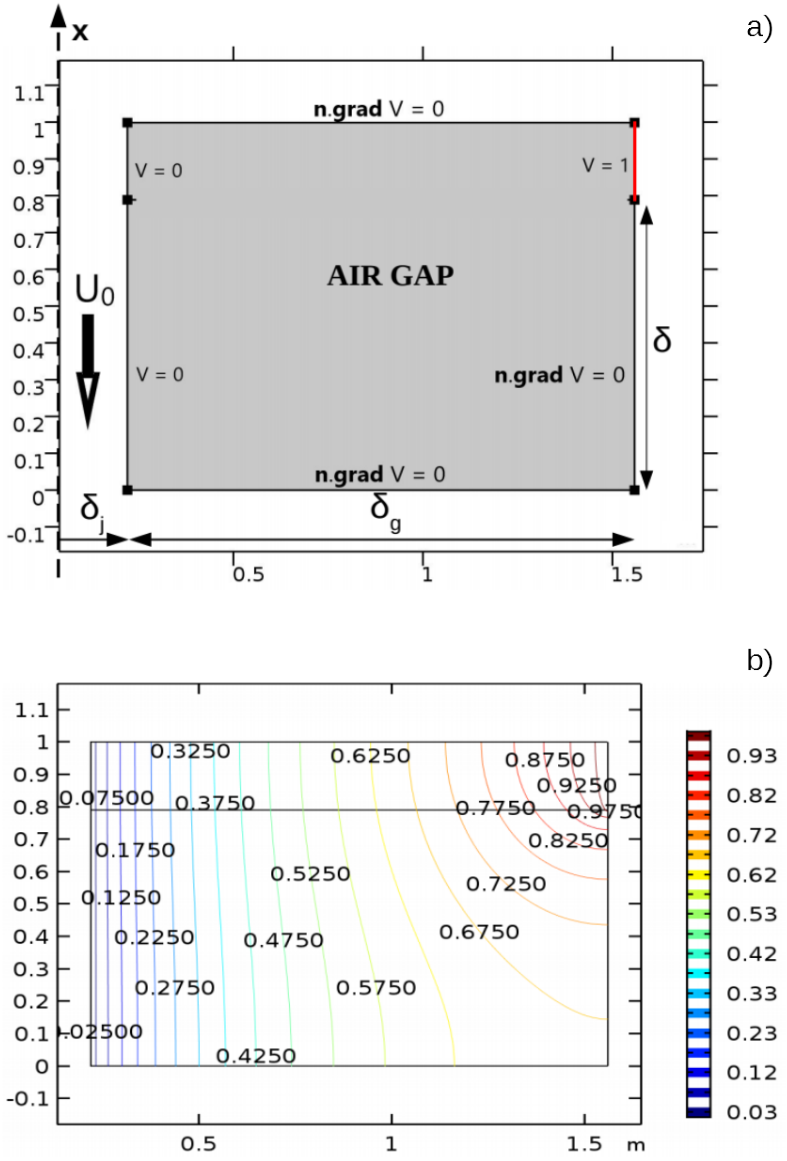

Figure 14. a) Geometry and boundary conditions for the non-dimensional electric potential. b) Equipotential lines and value of the non-dimensional electric potential in the air gap.

sandwiched between the outer boundary of the grounded jet and the inner boundary of the electrode stack. The fitted values of the coefficients, E_{ai}, E_{bi} (i^{th}-mode), consistently range between 0 and 1.

As illustrated in Fifs. 15a-b, various parametric tests performed over a consistent range of the aspect ratios, δ, δ_j and δ_g, demonstrate that the second mode coefficients (E_{a2}, E_{b2})

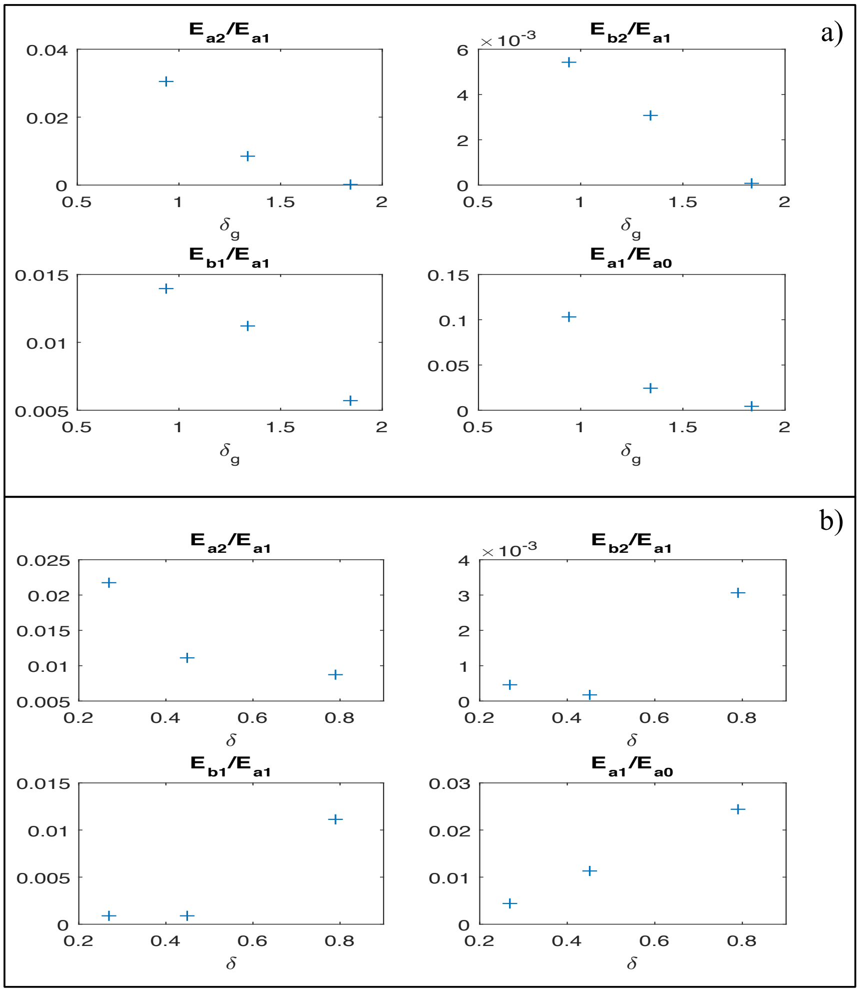

Figure 15. a) Coefficient ratios against δ_g ($\delta = 0.79$, $\delta_j = 0.22$). b) Coefficient ratios against δ ($\delta_g = 1.34$, $\delta_j = 0.22$).

remain negligibly small with respect to the first mode coefficients. Beyond this, only one single coefficient E_{a1} remains significant (Table V), which means that the electric field along the jet is essentially driven by a monochromatic distribution. Figures 16a-b display the curve fitting of the normal electric field distribution along the liquid jet, with the DC offset removed. For these simulations, just the aspect ratio δ_g is made to change ($\delta_g = 0.94$ in Fig. 16a, $\delta_g = 1.34$ in Fig. 16b).

One can note that a larger value of the aspect ratio δ_g consistently delivers a smaller modulation of the electric field. To conclude, the normal electric field at the interface is characterised by a harmonic distribution enhanced by a DC component, the latter of which does not contribute to the excitation of the deformation modes.

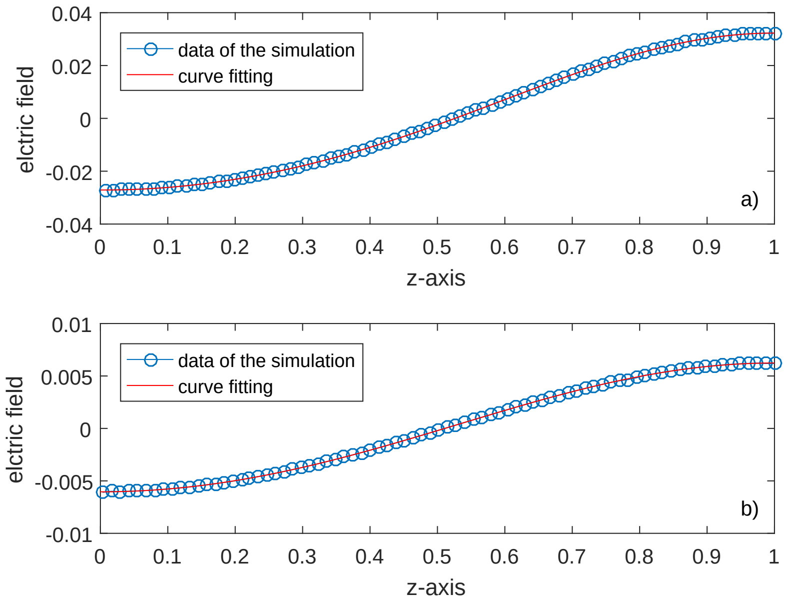

Figure 16. Curve fitting of the modulation of the normal eletric field for two cases: a) $\delta_j = 0.22$, $\delta_g = 0.94$ and $\delta = 0.79$; b) $\delta_j = 0.22$, $\delta_g = 1.34$ and $\delta = 0.79$.

	E_{a0}	E_{a1}	E_{b1}	E_{a2}	E_{b2}	k
Fig.16a: δ_g=0.94	4.352×10^{-4}	-2.955×10^{-2}	-2.517×10^{-3}	2.014×10^{-3}	1.029×10^{-3}	3.263
Fig.16b: δ_g=1.34	-5.107×10^{-5}	-6.139×10^{-3}	-1.086×10^{-5}	1.47×10^{-4}	2.21×10^{-6}	3.142

Table V. Values of the parameters in Eq. A6 as obtained from a curve fitting of the normal component of the electric field, $E_{n,s}$ ($\delta_j = 0.22$, $\delta = 0.79$).s

Appendix B: Derivation of the expressions for the radial disturbance and the normal velocity *r'*

1. Calculation of the functions r_α and r'_α

The radial perturbation r_α is only dependent on x. Equation (20a) can therefore be simplified as:

$$\frac{\partial^2 r_\alpha}{\partial x^2} = A_1\, k^{*2}\, \cos(k^*\, x). \tag{B1}$$

Considering boundary conditions (21) for the integration of (B1), the solutions for r_α and r'_α are found to write as:

$$r_\alpha(x) = A_1\,\left[1 - \cos\left(k^*\,x\right)\right], \tag{B2}$$

$$r'_\alpha(x) = A_1\,k^*\sin\left(k^*\,x\right). \tag{B3}$$

2. Calculation of the functions r_β and r'_β

The forcing term of Eq. (20b) is representative of a standing wave. It can also be written as two superimposed travelling waves:

$$\left(\frac{\partial}{\partial t} + \frac{\partial}{\partial x}\right)^2 \cdot r_\beta = \frac{A_1}{2}\,k^{*2}\,\left[\cos(2\omega_E\,t + k^*\,x) + \cos(2\omega_E\,t - k^*\,x)\right]. \tag{B4}$$

The complex notation $\hat{r}_\beta$, with $r_\beta = \Re\left(\hat{r}_\beta\right)$, is introduced so that Eq. (B4) writes in its complex form:

$$\left(\frac{\partial}{\partial t} + \frac{\partial}{\partial x}\right)^2 \cdot \hat{r}_\beta = \frac{A_1}{2}\,k^{*2}\,\left[e^{i\,(2\omega_E\,t + k^*\,x)} + e^{i\,(2\omega_E\,t - k^*\,x)}\right]. \tag{B5}$$

It must be kept in mind that r_β describes the growth of a radial perturbation travelling along the jet. A particular form for r (and therefore for r_β) can be inferred which is that of a progressive wave:

$$\hat{r}_\beta = F(x)\cdot e^{i\,(\omega\,t - k\,x)}, \tag{B6}$$

where F stands as a (complex) function to be determined.

By injecting (B6) into the equation (B5), it comes first for the left-hand term of the latter :

$$\begin{aligned}\left(\frac{\partial}{\partial t} + \frac{\partial}{\partial x}\right)^2 \cdot \hat{r}_\beta =& \frac{\partial^2}{\partial t^2}\left(F(x)\cdot e^{i\,(\omega\,t - k\,x)}\right) + \frac{\partial^2}{\partial x^2}\left(F(x)\cdot e^{i\,(\omega\,t - k\,x)}\right) + \\ &+ 2\,\frac{\partial^2}{\partial x\,\partial t}\left(F(x)\cdot e^{i\,(\omega\,t - k\,x)}\right) \\ &+\ 2\,i\,\omega\left[F' - i\,k\,F\right]\cdot e^{i\,(\omega\,t - k\,x)} \\ =& \left[-\omega^2\,F + F'' - 2\,i\,k\,F' - k^2\,F + 2\,i\,\omega\,F' + 2\,\omega\,k\,F\right]\cdot e^{i\,(\omega\,t - k\,x)}.\end{aligned} \tag{B7}$$

The previous equation may seem tedious to solve. Nevertheless a relation between the $\tilde{\omega}$ pulsation and the $\tilde{k}$ wave number can be put forward assuming that the radial perturbation is transported by inertia along the jet. In other words, the ratio of the angular frequency to the wave number is supposed equal to the mean velocity of the liquid jet, U_0:

$$\tilde{k} \cdot U_0 = \tilde{\omega} \Leftrightarrow k = \omega.$$

As a consequence, Eq. (B7) simplifies to:

$$\left(\frac{\partial}{\partial t} + \frac{\partial}{\partial x}\right)^2 \cdot \hat{r}_\beta = F^{''} \cdot e^{i\,(\omega\,t - k\,x)}.$$

From this, one can rewrite the equation (B5):

$$F^{''}(x) = \frac{A_1}{2}\,k^{*2}\,\left[e^{i\,(2\omega_E\,t + k^*\,x)} + e^{i\,(2\omega_E\,t - k^*\,x)}\right] \cdot e^{-i\,(\omega\,t - k\,x)}.$$

Assuming that $\omega = 2\,\omega_E$, one obtains successively:

$$\begin{aligned} F^{''}(x) &= \frac{A_1}{2}\,k^{*2}\,\left[e^{i\,k^*\,(L+1)\,x} + e^{i\,k^*\,(L-1)\,x}\right], \\ F^{'}(x) &= \frac{A_1}{2}\,k^*\,\left[\frac{1}{i\,(L+1)}\,e^{i\,k^*\,(L+1)\,x} + \frac{1}{i\,(L-1)}\,e^{i\,k^*\,(L-1)\,x}\right] + C1, \end{aligned}$$

where C1 is a constant parameter to be determined. From boundary conditions (21), $F^{'}$ is found to write:

$$F^{'}(x) = \frac{-i\,A_1}{2\,(L^2-1)}\,k^*\,\left[(L-1)\,e^{i\,k^*\,(L+1)\,x} + (L+1)\,e^{i\,k^*\,(L-1)\,x} - 2\,L\right].$$

By integrating once again the latter equation and taking into account the boundary conditions (21), one gets:

$$F(x) = \frac{-A_1}{2\,(L^2-1)}\,\left[\frac{(L-1)^2\,e^{i\,k^*\,(L+1)\,x} + (L+1)^2\,e^{i\,k^*\,(L-1)\,x} - 2\,(L^2+1)}{(L^2-1)} - 2\,L\,i\,k^*\,x\right].$$

Considering (B6), the function $\hat{r}_\beta$, and therefore the function $\hat{r}_\beta^{'}$, write finally as:

$$\begin{aligned} \hat{r}_\beta =& \frac{-A_1}{2\,(L^2-1)}\left[\frac{1}{(L^2-1)}\left((L-1)^2\,e^{i\,k^*\,(L+1)\,x} + (L+1)^2\,e^{i\,k^*\,(L-1)\,x} - 2\,(L^2+1)\right) + \right. \\ & \left. - 2\,L\,i\,k^*\,x\right] \cdot e^{i\,(\omega\,t - k\,x)}, \qquad \text{(B8)} \\ \hat{r}_\beta^{'} =& \frac{-i\,A_1}{2\,(L^2-1)}\,k^*\,\left[(L-1)\,e^{i\,k^*\,(L+1)\,x} + (L+1)\,e^{i\,k^*\,(L-1)\,x} - 2\,L\right] \cdot e^{i\,(\omega\,t - k\,x)}. \qquad \text{(B9)} \end{aligned}$$

Appendix C: Calculation of the breakup length

1. General solution

Breakup is set to arise downstream after the electric stress has vanished (zone 2). Hence, the radial deformation is supposed well described from Eq. (11). Nevertheless, there is still the need for evaluating the boundary conditions r_0 and $r_0^{'}$ at the junction between zones 1 and 2 (at $x = x_p$). To this end, use is made of Eqs. (22)–(25) in order to express matching conditions in $x = x_p$ for the radial deformation r and the radial component of the surface velocity r'. By setting the origin of the x axis at the beginning of zone 1, the junction between zones 1 and 2 is located at $\tilde{x}_p = 2\,n\,d$ with n, the number of electrodes (Fig. 1). By resizing $\tilde{x}_p$ such that $x_p = \frac{\tilde{x}_p}{d}$, it comes out that $x_p = 2\,n$.

By calculating successively r_α, $r_\alpha^{'}$, $\hat{r}_\beta$ and $\hat{r}_\beta^{'}$ in $x = x_p$, we obtain after tedious but simple calculations:

$$r_\alpha\,(x_p) = r_\alpha^{'}\,(x_p) = 0,$$

$$\hat{r}_\beta(x_p) = \frac{-2\,A_1}{(L^2-1)}\left[\frac{(L^2+1)\,e^{i\,k^*\,L\,n}}{(L^2-1)}\,\sin(k^*\,L\,n) - L\,i\,k^*\,n\right]\cdot e^{i\,(\omega\,t - k\,x_p)}, \tag{C1}$$

and,

$$\hat{r}_\beta^{'}(x_p) = \frac{2\,L\,A_1}{L^2-1}\,k^*\,e^{i\,k^*\,L\,n}\,\sin(k^*\,L\,n)\cdot e^{i\,(\omega\,t-k\,x_p)}. \tag{C2}$$

Note that the α components of the jet disturbance do not affect the stability of the jet. To take into account the matching conditions of the perturbation in $x = x_p$, it is sufficient to extract the module from the two previous equations (C1)–(C2).

Considering also the distance between the origin of the x-axis and the beginning of zone 2, together with the Taylor assumption, $\tilde{x} = U_0\,\tilde{t}$, a time delay t_p can be injected in Eq. (11) and the solution for the radial disturbance writes:

$$\tilde{r}(x,t) = \frac{1}{2}\left[\tilde{r}_0 + \frac{R_0\,\tilde{r}_0'}{\mu\,U_0}\right]\cdot \mathrm{e}^{\frac{\mu\,U_0\,(\tilde{t}-\tilde{t}_p)}{R_0}}\,\cos\Big((\tilde{x} - U_0\,(\tilde{t}-\tilde{t}_p))\cdot\tilde{k}\Big), \tag{C3}$$

or alternatively,

$$\tilde{r}(x,t) = \frac{1}{2}\left[\tilde{r}_0 + \frac{R_0\,\tilde{r}_0'}{\mu\,U_0}\right]\cdot \mathrm{e}^{\frac{\mu\,(\tilde{x}-\tilde{x}_p)}{R_0}}\,\cos\Big((U_0\,\tilde{t} - (\tilde{x}-\tilde{x}_p))\cdot\tilde{k}\Big), \tag{C4}$$

with,

$$\tilde{r}_0 = \tilde{r}_0 \cdot |\hat{r}(x_p)|, \tag{C5a}$$

$$\tilde{r}_0' = \tilde{r}_0 \, \frac{U_0}{d} \cdot |\hat{r}'(x_p)|. \tag{C5b}$$

However, we can simplify the initial radial perturbation in zone 2. Considering that the term which depends on r_0' generally dominates over the initial perturbation, Eq. (C4) can be reduced to:

$$\tilde{r}(x,t) = \frac{R_0 \, \tilde{r}_0'}{2 \, \mu \, U_0} \cdot \mathrm{e}^{\dfrac{\mu \, (\tilde{x} - \tilde{x}_p)}{R_0}} \cos\Big((U_0 \, \tilde{t} - (\tilde{x} - \tilde{x}_p)) \cdot \tilde{k} \Big) \, , \tag{C6}$$

from which a breakup length can be calculated (see also Eq. 12):

$$\tilde{l}_{2rupt} = \frac{R_0}{\mu} \ln \left(\frac{2 \, \mu \, U_0}{\tilde{r}_0'} \right). \tag{C7}$$

After calculations, it can be demonstrated that:

$$\frac{\tilde{l}_{rupt}}{R_0} = \frac{1}{\mu} \ln \left(\frac{2 \sqrt{1 - (\pi \, \delta_j \, L)^2}}{\sqrt{2} \, \sqrt{We} \, Eu_E \cdot E_0 \, E_{a1}} \cdot \frac{|(L^2 - 1)|}{|\sin(\pi \, L \, n)|} \right). \tag{C8}$$

2. Case L=1

One can determine the breakup length when the frequency ratio L is equal to 1 since in this case, the influence ratio (34) becomes:

$$\frac{|\sin(\pi \, L \, n)|}{|(L^2 - 1)|} \underset{L \mapsto 1}{\longmapsto} \frac{n \, \pi}{2}, \tag{C9}$$

The breakup length is therefore minimised when the frequency of the electric field is equal to the synchronization frequency (L=1), especially when the number of electrodes, n, is large. In this optimised case, Eq. (C8) simplifies to:

$$\frac{\tilde{l}_{2rupt}}{R_0} = \frac{1}{\mu} \ln \left(\frac{4 \sqrt{1 - (\pi \, \delta_j)^2}}{\pi \, n \, \sqrt{2} \, \sqrt{We} \, Eu_E \cdot E_0 \, E_{a1}} \right). \tag{C10}$$

Appendix D: Typical snapshots

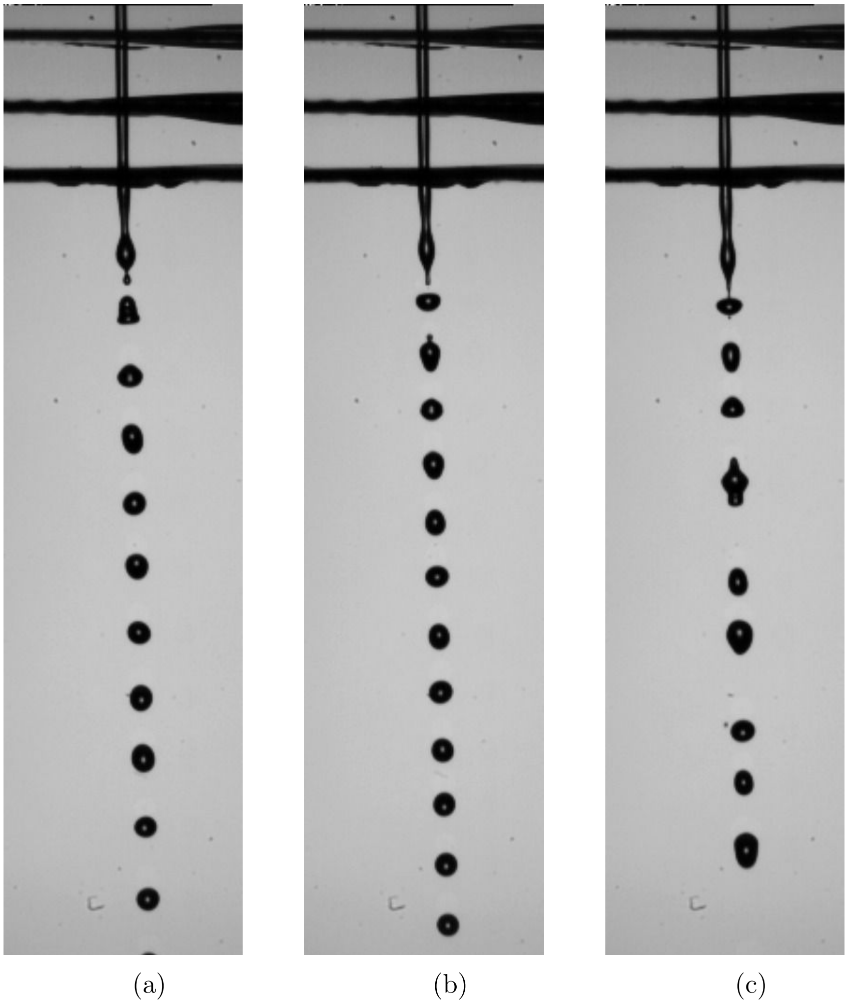
(a) (b) (c)

Figure 17. (Multimedia view) Electrically-induced jet atomisation for different frequencies at a synchronisation wavelength λ_{sync} of 2.35mm ($\tilde{k}\, R_0 = 0.53$) and a Weber number of 5.9 (see also Table III). (a) Electrostatic actuation in the frequency range #1. (b) frequency range #2. (c) Signal frequency of 430 Hz (size dispersion).

REFERENCES

[1] G D Martin, S D Hoath, and I M Hutchings. Inkjet printing - the physics of manipulating liquid jets and drops. *Journal of Physics: Conference Series*, 105:012001, mar 2008.

[2] S. H. Kang, S. Kim, D. K. Sohn, and H. S. Ko. Analysis of drop-on-demand piezo inkjet performance. *Physics of Fluids*, 32(2):022007, 2020.

[3] E. Antonopoulou, O. G. Harlen, M. Rump, T. Segers, and M. A. Walkley. Effect of surfactants on jet break-up in drop-on-demand inkjet printing. *Physics of Fluids*, 33(7):072112, 2021.

[4] Mehrzad Roudini, Dennis Niedermeier, Frank Stratmann, and Andreas Winkler. Droplet generation in standing-surface-acoustic-wave nebulization at controlled air humidity. *Phys. Rev. Applied*, 14:014071, Jul 2020.

[5] S. A. Elrod, B. Hadimioglu, B. T. Khuri-Yakub, E. G. Rawson, E. Richley, C. F. Quate, N. N. Mansour, and T. S. Lundgren. Nozzleless droplet formation with focused acoustic beams. *Journal of Applied Physics*, 65(9):3441–3447, 1989.

[6] B. Hadimioglu, S. A. Elrod, D. L. Steinmetz, M. Lim, J. C. Zesch, B. T. Khuri-Yakub, E. G. Rawson, and C. F. Quate. Acoustic ink printing. In *IEEE 1992 Ultrasonics Symposium Proceedings*, pages 929–935 vol.2, 1992.

[7] A. Amirzadeh Goghari and S. Chandra. Producing droplets smaller than the nozzle diameter by using a pneumatic drop-on-demand droplet generator. *Experiments in Fluids*, 44(1):105–114, 2008.

[8] J. M. Crowley. Electrohydrodynamic droplet generators. *Journal of Electrostatics*, 14(2):121 – 134, 1983.

[9] D. W. Hrdina and J. M. Crowley. Drop-on-demand operation of continuous jets using ehd techniques. *IEEE Transactions on Industry Applications*, 25(4):705–710, July 1989.

[10] A. Atten and S. Oliveri. Charging of drops formed by circular jet breakup. *Journal of Electrostatics*, 29(1):73 – 91, 1992.

[11] H. González, F. J. García, and A. Castellanos. Stability analysis of conducting jets under ac radial electric fields for arbitrary viscosity. *Physics of Fluids*, 15(2):395–407, 2003.

[12] G. Brenn. *Droplet Stream Generator*, pages 603–624. Springer, in: ashgriz n. (eds) edition, 2011.

[13] L. L. F. Agostinho, C. U. Yurteri, E. C. Fuchs, and J. C. M. Marijnissen. Monodisperse water microdroplets generated by electrohydrodynamic atomization in the simple-jet mode. *Applied Physics Letters*, 100(24):244105, 2012.

[14] J. Raisin, P. Atten, and J-L. Reboud. A novel actuation technique for the on-demand injection of charge-free conducting droplets in a viscous dielectric liquid. *Experiments in*

Fluids, 54(3):1473, 2013.

[15]Y. Xia. Electrohydrodynamic droplet injection method into model oil. *AIP Advances*, 9(10):105309, 2019.

[16]Shiqi Yang, Zhentao Wang, Qian Kong, and Bin Li. Varicose-whipping instabilities transition of an electrified micro-jet in electrohydrodynamic cone-jet regime. *International Journal of Multiphase Flow*, 146:103851, 2022.

[17]R. Malk, A. Rival, Y. Fouillet, and L. Davoust. EWOD in Coplanar Electrode Configurations. In *ASME 2010 8th International Conference on Nanochannels, Microchannels, and Minichannels: Parts A and B*, pages 239–248, 08 2010.

[18]R. Malk, J. Theisen, Y. Fouillet, and L. Davoust. Ewod-driven stirring in lab-on-a-chips: Dependence on the electrodes' geometry. *Microelectronic Engineering*, 97:306 – 310, 2012. Micro- and Nano-Engineering (MNE) 2011, selected contributions: Part I.

[19]J. Theisen and L. Davoust. Dual-frequency electrowetting: Application to drop evaporation gauging within a digital microsystem. *Langmuir*, 28(1):1041–1048, 2012.

[20]J. Theisen and L. Davoust. Mass transfer enhancement and surface functionalization in digital microfluidics using ac electrowetting: the smaller, the better. *Microfluidics and Nanofluidics*, 18(5):1373–1389, 2015.

[21]E. Samiei, M. Tabrizian, and Mina H. A review of digital microfluidics as portable platforms for lab-on a-chip applications. *Lab Chip*, 16:2376–2396, 2016.

[22]L. Davoust, C. Abs da Cruz, and J. Theisen. On the use of ac electrowetting for biosensing based on dynamic contact angle. *Sensors and Actuators B: Chemical*, 236:849 – 857, 2016.

[23]Bhaskarjyoti Sarma, Sunny Kumar, Amaresh Dalal, Dipankar N. Basu, and Dipankar Bandyopadhyay. Electric-discharge-mediated jetting, crowning, bursting, and atomization of a droplet. *Phys. Rev. Applied*, 15:014005, Jan 2021.

[24]N R Lindblad and J M Schneider. Production of uniform-sized liquid droplets. *Journal of Scientific Instruments*, 42(8):635–638, aug 1965.

[25]M. Orme, K. Willis, and T-V. Nguyen. Droplet patterns from capillary stream breakup. *Physics of Fluids*, 5:80–90, 01 1993.

[26]G. Perçin and B. T. Khuri-Yakub. Piezoelectric droplet ejector for ink-jet printing of fluids and solid particles. *Review of Scientific Instruments*, 74(2):1120–1127, 2003.

[27]J. M. Meacham, M. J. Varady, F. L. Degertekin, and A. G. Fedorov. Droplet formation and ejection from a micromachined ultrasonic droplet generator: Visualization and scaling.

Physics of Fluids, 17(10):100605, 2005.

[28]H. Dong, W. W. Carr, and J. F. Morris. An experimental study of drop-on-demand drop formation. *Physics of Fluids*, 18(7):072102, 2006.

[29]A. Bransky, N. Korin, M. Khoury, and S. Levenberg. A microfluidic droplet generator based on a piezoelectric actuator. *Lab Chip*, 9:516–520, 2009.

[30]D. M. Harris, T. Liu, and J. W. M. Bush. A low-cost, precise piezoelectric droplet-on-demand generator. *Experiments in Fluids*, 56(4):83, 2015.

[31]H. Li, J. Liu, K. Li, and Y. Liu. Piezoelectric micro-jet devices: A review. *Sensors and Actuators A: Physical*, 297:111552, 2019.

[32]Seung-Hwan Kang, San Kim, Dong Kee Sohn, and Han Seo Ko. Analysis of drop-on-demand piezo inkjet performance. *Physics of Fluids*, 32(2):022007, 2020.

[33]E. Antonopoulou, O. G. Harlen, M. A. Walkley, and N. Kapur. Jetting behavior in drop-on-demand printing: Laboratory experiments and numerical simulations. *Phys. Rev. Fluids*, 5:043603, Apr 2020.

[34]Jiaqing Chang, Fan Jiang, Ziteng Liu, Dachang Zhu, and Teng Shen. Simulation and experimental study on droplet breakup modes and redrawing of their phase diagram. *Physics of Fluids*, 33(8):082105, 2021.

[35]Lord Rayleigh. On the instability of jets. *Proceedings of the London Mathematical Society*, s1-10(1):4–13, 1878.

[36]J. Choi, Y-J. Kim, S. Lee, S. U. Son, H. S. Ko, V. D. Nguyen, and D. Byun. Drop-on-demand printing of conductive ink by electrostatic field induced inkjet head. *Applied Physics Letters*, 93(19):193508, 2008.

[37]M. P. Borthakur, G. Biswas, and D. Bandyopadhyay. Dynamics of drop formation from submerged orifices under the influence of electric field. *Physics of Fluids*, 30(12):122104, 2018.

[38]X. Zhang and O. A. Basaran. Dynamics of drop formation from a capillary in the presence of an electric field. *Journal of Fluid Mechanics*, 326:239–263, 1996.

[39]J. Xie, J. Jiang, P. Davoodi, M.P. Srinivasan, and C-H. Wang. Electrohydrodynamic atomization: A two-decade effort to produce and process micro-/nanoparticulate materials. *Chemical Engineering Science*, 125:32 – 57, 2015. Pharmaceutical Particles and Processing.

[40]A. Castellanos. *Electrohydrodynamics*. Springer, 1998.

[41] G. Artana, H. Romat, and G. Touchard. Study of a high-velocity liquid jet stressed by an electric field. *Physics of Fluids*, 10(11):2922–2931, 1998.

[42] Soucemarianadin A. Spohn A., Atten P. and Dunand A. Theoretical and experimental study of multi-electrode electrohydrodynamic stimulation of liquid jets. In *Proc. of IS and T's Ninth InternationalCongress on Advances in Non-Impact Printing Technologies*, 1993.

[43] Jens Eggers and Emmanuel Villermaux. Physics of liquid jets. *Reports on Progress in Physics*, 71(3):036601, feb 2008.

[44] H. C. Lee. Drop formation in a liquid jet. *IBM Journal of Research and Development*, 18(4):364–369, July 1974.

[45] J.C. Slattery, L. Sagis, and E.-S. Oh. *Interfacial transport phenomena.* Springer, 2nd edition, 2007.